CROSS-CORRELATION WEAK LENSING OF SDSS GALAXY CLUSTERS II: CLUSTER DENSITY PROFILES AND THE MASS–RICHNESS RELATION

David E. Johnston,[1,2] Erin S. Sheldon,[3] Risa H. Wechsler,[8] Eduardo Rozo,[9] Benjamin P. Koester, [4,11] Joshua A. Frieman,[4,10,11] Timothy A. McKay,[5,6,7] August E. Evrard,[5,6,7] Matthew R. Becker [5] James Annis, [10]
(Received; Accepted)
Draft version February 1, 2008

ABSTRACT

We interpret and model the statistical weak lensing measurements around 130,000 groups and clusters of galaxies in the Sloan Digital Sky Survey presented by Sheldon et al. (2007). We present non-parametric inversions of the 2D shear profiles to the mean 3D cluster density and mass profiles in bins of both optical richness and cluster i-band luminosity. Since the mean cluster density profile is proportional to the cluster–mass correlation function, the mean profile is spherically symmetric by the assumptions of large-scale homogeneity and isotropy. We correct the inferred 3D profiles for systematic effects, including non-linear shear and the fact that cluster halos are not all precisely centered on their brightest galaxies. We also model the measured cluster shear profile as a sum of contributions from the brightest central galaxy, the cluster dark matter halo, and neighboring halos. We infer the relations between mean cluster virial mass and optical richness and luminosity over two orders of magnitude in cluster mass; the virial mass at fixed richness or luminosity is determined with a precision of $\sim 13\%$ including both statistical and systematic errors. We also constrain the halo concentration parameter and halo bias as a function of cluster mass; both are in good agreement with predictions from N-body simulations of LCDM models. The methods employed here will be applicable to deeper, wide-area optical surveys that aim to constrain the nature of the dark energy, such as the Dark Energy Survey, the Large Synoptic Survey Telescope and space-based surveys.

Subject headings: gravitational lensing – galaxies: clusters – large-scale structure – cosmology:observations – galaxies: halos – dark matter

1. INTRODUCTION

Clusters of galaxies are among the most promising probes of cosmology and of the physics of structure formation. Theoretical calculation (Gunn & Gott 1972; Press & Schechter 1974) followed by numerical simulations with ever-increasing resolution (e.g. Navarro et al. 1997; Evrard et al. 2002) have led to a robust, quantitative framework for the understanding of the non-linear growth, collapse, and evolution of dark-matter halos. Rich clusters are now confidently associated with the most massive, collapsed halos. N-body simulations predict the abundance of halos

[1] Jet Propulsion Laboratory, 4800 Oak Grove Drive, Pasadena CA, 91109, email davej@astro.caltech.edu
[2] California Institute of Technology, 1200 East California Blvd, Pasadena, CA 91125
[3] Center for Cosmology and Particle Physics,Department of Physics, New York University, 4 Washington Place, New York, NY, 10003
[4] Department of Astronomy and Astrophysics, The University of Chicago, 5640 South Ellis Avenue, Chicago, IL 60637
[5] Physics Department, University of Michigan, Ann Arbor, MI 48109
[6] Astronomy Department, University of Michigan, Ann Arbor, MI 48109
[7] Michigan Center for Theoretical Physics, Ann Arbor, MI, 48109
[8] Kavli Institute for Particle Astrophysics and Cosmology, Physics Department, and Stanford Linear Accelerator Center, Stanford University, 382 Pueblo Mall, Stanford, CA, 94305
[9] CCAPP Fellow, The Ohio State University, Columbus, Ohio 43210
[10] Center for Particle Astrophysics, Fermi National Accelerator Laboratory, P.O. Box 500, Batavia, IL 60510
[11] Kavli Institute for Cosmological Physics, The University of Chicago, 5640 South Ellis Avenue, Chicago, IL 60637

(Sheth & Tormen 1999; Warren et al. 2006), their density profiles (Navarro et al. 1997), their concentrations (Bullock et al. 2001; Eke et al. 2001; Wechsler et al. 2002; Macciò et al. 2007; Neto et al. 2007), and their large-scale clustering (Kaiser 1984; Mo et al. 1996; Seljak & Warren 2004a; Wetzel et al. 2007). The abundance of dark matter halos is a strong function of the cosmological parameters, especially σ_8, the normalization of the matter power spectrum (White et al. 1993; Viana & Liddle 1999; Bahcall et al. 2003). Moreover, the evolution of the cluster abundance with redshift is quite sensitive to the equation of state of the dark energy (Haiman et al. 2001; Huterer & Turner 2001; Newman et al. 2002; Levine et al. 2002). An accurate measurement of the cluster abundance can thus be used to determine cosmological parameters.

However, to exploit clusters as cosmological probes requires knowledge of the relation between their observable properties and their masses — so far, a measurement of the cluster mass-observable relation with the necessary robustness and precision has been lacking. Various methods have been employed to detect clusters and to estimate their masses; each has advantages and disadvantages, and it is likely that in the future they will be increasingly used in combination.

Measurements of X-ray flux and temperature profiles, combined with the assumption that the X-ray emitting gas is in hydrostatic equilibrium (HSE) in a spherically symmetric gravitational potential, can be used to infer cluster mass profiles (Reiprich & Böhringer 2002; Nagai et al. 2007). However, recent XMM-Newton and Chandra data (Markevitch & Vikhlinin 2007) have

shown that a fraction of clusters have complex luminosity and temperature structure, perhaps associated with recent merger or AGN activity, calling into question the spherical HSE assumption in those cases (Evrard et al. 1996). In addition, inference of the mass profile in HSE requires measurement of the radial gas temperature profile, which in turn requires large numbers of X-ray photons, so only nearby (Sanderson & Ponman 2004) or very massive clusters (Allen et al. 2007) are suitable for this treatment. Future X-ray observatories such as XEUS and Constellation-X will have greatly improved sensitivity and will therefore be able to probe lower-mass clusters with this technique.

The Sunyaev-Zel'dovich (SZ) effect, another gas-based method of detecting clusters (Grego et al. 2001; Carlstrom et al. 2002), has the advantage of being essentially redshift independent. Theoretically, the integrated Sunyaev-Zel'dovich flux increment is tightly correlated with cluster mass (Motl et al. 2005; Nagai 2006), and the slope of the relation appears to be insensitive to gas dynamics in cluster cores. Challenges for this technique (Hallman et al. 2006) include the identification and removal of contamination by radio point sources (Vale & White 2006). Recent SZ measurements (LaRoque et al. 2006) will soon be supplemented by studies from the APEX-SZ, the Sunyaev-Zel'dovich Array, and by large surveys with, e.g., the Atacama Cosmology Telescope and the South Pole Telescope.

Dynamical cluster mass estimates, using the estimated velocity dispersion of cluster galaxies, are also useful, but they require many spectroscopic measurements per cluster. The interpretation of the velocity dispersion as a measure of the cluster mass also usually requires assumptions about dynamical equilibrium and about the distribution of galaxy orbits (velocity anisotropy), although techniques to bypass these assumptions by simulating cluster galaxy dynamics directly have also been employed (Evrard et al. 2007). Dynamical estimates are also subject to uncertainty in the relation between galaxy and dark matter velocity dispersion, called velocity bias, which in principle requires inclusion of gas dynamics and stellar feedback to properly simulate. Recent work indicates that this effect is small, but depends on the type of galaxy sampled (e.g. Nagai & Kravtsov 2005; Diemand et al. 2004).

Gravitational lensing has proven an effective tool in probing the masses of clusters. Due to the simplicity of the gravitational physics of lensing, it has become one of the most secure ways of demonstrating the existence of dark matter (Clowe et al. 2006). Strong lensing, using multiple images and arcs, can provide precise cluster mass estimates on small scales (Hammer 1991; Kneib et al. 1996). However, strong lensing only occurs in very massive clusters; moreover, strong lensing clusters may not be typical of clusters of their mass, since the existence of arcs requires high central mass concentrations. Weak lensing has been used to construct projected mass maps of clusters to larger scales (e.g. Fahlman et al. 1994; Tyson & Fischer 1995; Luppino & Kaiser 1997; Clowe et al. 1998; Joffre et al. 2000; Irgens et al. 2002; Cypriano et al. 2004; Bradač et al. 2006). However, individual weak lensing cluster mass estimates inferred from shear measurements are subject to $\sim$ 20% uncertainties (Metzler et al. 1999, 2001; Hoekstra 2003;

de Putter & White 2005), since they are sensitive to all mass along the line of sight to the source galaxies, not just that associated with the cluster. Weak lensing mass estimates are also affected by the "mass-sheet" degeneracy (Bradač et al. 2004): adding a constant mass sheet to the 2D mass density does not change the weak lensing shear.

Fortunately, to use clusters to constrain cosmological parameters, determination of the masses of *individual* clusters is unnecessary, since cosmological predictions of structure formation are statistical in nature. Cosmological theory robustly predicts the halo mass function $n(M; z, \theta_i)$, where θ_i stands for a vector of cosmological parameters. Astronomical observations measure the abundance of clusters sorted by some observable property O, $n(O; z)$. To compare theoretical predictions with observations, we need to measure or constrain the conditional probability distribution, $P(O|M; z)$, that a dark matter halo of mass M at redshift z will be observed as a cluster with observable O in a given survey, including selection effects and biases. This is the approach employed, e.g., by Rozo et al. (2007a), who adopt the halo occupation distribution (HOD) description of this conditional probability distribution and marginalize over the HOD model parameters to arrive at cosmological constraints. Alternatively, one could rely on, e.g., hydrodynamic or semi-analytic galaxy formation models to directly predict $n(O; z, \theta_i)$, but the theoretical uncertainties — which are roughly captured in the HOD model — are still large.

The method of "cross-correlation weak lensing" provides a direct estimate of the mean mass for clusters with some observable property O and therefore an important constraint on the probability distribution $P(O|M; z)$ needed to connect cosmological theory with cluster observations. Cross-correlation lensing consists of stacking the weak lensing signal from a large number of objects, selected by some property O, to measure the average shear profile with high signal-to-noise. By combining the signal from many lenses, the error on the mean shear profile and on the inferred mean mass can in principle be reduced to the sub-percent level; in that limit, systematic errors of interpretation start to dominate. Since less massive objects are more abundant in the Universe, cross-correlation lensing can be used over a very wide range of lens masses — from massive clusters down to galaxies, where it is referred to as galaxy-galaxy lensing (Tyson et al. 1984; Brainerd et al. 1996; Fischer et al. 2000; Sheldon et al. 2004; Mandelbaum et al. 2006). Because the method corresponds to a statistical measurement of the lens-mass cross-correlation function (see §3), the inferred mean masses are insensitive to *uncorrelated* mass along the line of sight to the source galaxies. For cluster-scale lenses, the mean effects of *correlated* mass along the line of sight, e.g., in neighboring clusters or filaments, are generally negligible out to scales comparable to the cluster virial radius. Moreover, their effects can be measured and modeled, as we show in §4. As a result, cross-correlation lensing is essentially free of the projection effects that plague individual cluster lens mass estimates.

In Sheldon et al. (2007) (hereafter Paper I), we presented average shear profiles from cross-correlation weak lensing measurements around $\sim$ 130,000 clusters of galaxies from the Sloan Digital Sky Survey (SDSS,

York et al. 2000). These clusters were selected from the maxBCG cluster catalog described in Koester et al. (2007b); the maxBCG cluster finding algorithm, based on the red sequence of early-type cluster galaxies, is described in Koester et al. (2007a).

In this paper, we analyze the detected lensing signal presented in Paper I and model the features seen in the shear profiles. In §2 we summarize the relevant results from Paper I. In §3 we apply the non-parametric inversions of Johnston et al. (2007) to infer the mean 3D cluster mass density and aperture mass profiles in bins of optical richness and luminosity (see §2.1). These inverted density and mass profiles, however, *cannot* be directly interpreted as profiles of dark matter halos. In §4, we discuss why this is so and develop a parameterized model which includes the effects of: displacement of the center of the cluster halo from the brightest cluster galaxy (BCG); non-linear shear corrections; lensing by the central BCG; and lensing by neighboring clusters and structures. When these effects are included, we find that the inferred halo profiles are well fit by the universal dark matter profiles of Navarro, Frenk & White (Navarro et al. 1997). In the context of this model, we estimate the average halo virial mass, M_{200}, as a function of cluster galaxy richness and total galaxy luminosity. We infer the mean halo concentration and halo bias as a function of M_{200} and find them to be in good agreement with the predictions of N-body simulations for the standard LCDM cosmology. In §6 we compare the inferred mean halo masses vs. galaxy richness to recent dynamical mass estimates from measured velocity dispersions for the same cluster sample (Becker et al. 2007); the two mass estimates agree very well, with the lensing estimates having smaller errors. We conclude by discussing some cosmological applications of these results as well as applications in future optical surveys.

For computing distances and, where needed, the linear power spectrum of density perturbations, we use a spatially flat cosmological model with a cosmological constant and cold dark matter (LCDM) with scaled CDM density $\Omega_m = 0.27$, baryon density $\Omega_b = 0.045$, scaled Hubble parameter $h = 0.71$ (for the linear power spectrum not distances) and primordial spectral index $n_s = 0.95$. The linear power spectrum amplitude σ_8 is left free except where specified. We employ the linear transfer function of Eisenstein and Hu (Eisenstein & Hu 1998). This model (with $\sigma_8 = 0.8$) fits both the WMAP third-year data Spergel et al. (2007) and the SDSS luminous red galaxy (LRG) clustering data (Eisenstein et al. 2005). All distances in this paper are in *physical* not *comoving* units of $h^{-1}Mpc$.

2. WEAK LENSING SHEAR MEASUREMENTS

The methods of measuring the weak lensing signal are described in detail in Paper I. We briefly summarize some of the important features here. For any projected mass distribution, the azimuthally averaged tangential shear at projected radius R from the center of the distribution is given by $\gamma(R) = \Delta\Sigma(R)/\Sigma_{crit} \equiv [\overline{\Sigma}(< R) - \overline{\Sigma}(R)]/\Sigma_{crit}$, where $\Sigma(R)$ is the 2D projected mass density at radius R, $\overline{\Sigma}(< R)$ is the average of Σ inside a disk of radius R, $\overline{\Sigma}(R)$ is the azimuthal average of $\Sigma(R)$ in a thin annulus of radius R, and the critical density for strong lensing is given

Bin number	N_{200}	Number of clusters per bin
1	3	58788
2	4	27083
3	5	14925
4	6	8744
5	7	5630
6	8	3858
7	9-11	6196
8	12-17	4427
9	18-25	1711
10	26-40	787
11	41-70	272
12	71-220	47

NOTE. — The catalog is divided into 12 N_{200} richness bins. This table shows the boundaries of N_{200} values and the number of clusters for each bin.

by $\Sigma_{crit} \equiv c^2/(4\pi G) \; D_S/(D_L D_{LS})$, with D_S, D_L, D_{LS} the angular diameter distances from the observer to the source, to the lens, and between the lens and source, respectively. These distances are cosmology-dependent functions of redshift. Paper I presents average profiles of $\Delta\Sigma(R)$ for maxBCG clusters binned by cluster galaxy number, N_{200}, and by optical luminosity L_{200}. For these measurements, the radius R is defined with respect to the position of the BCG; see §4.3 for further discussion of this point.

2.1. Richness and Luminosity measures N_{200} and L_{200}

Although the richness and luminosity measures N_{200} and L_{200} are discussed in detail in Paper I, here we emphasize some of their important features to avoid possible confusion. N_{200} and L_{200} are the galaxy number and total i-band luminosity measured within a projected radius we call r_{200}^{gals}, in both cases counting only red-sequence galaxies with luminosities larger than $0.4L_*$ and satisfying other selection criteria (see Koester et al. 2007a for details). This radius is *not* by definition, equivalent to the r_{200} defined by the mass (Eqn. 4), which can in principle be measured directly from lensing, since r_{200} is not known prior to performing the weak lensing analysis. Instead, r_{200}^{gals} is determined by first measuring the number of galaxies, N_{gal}, within a fixed 1 h^{-1} Mpc aperture and calculating $r_{200}^{gals} = 0.156 \; N_{gal}^{0.6} \; h^{-1}$ Mpc, as discussed in Hansen et al. (2005). Nevertheless, we find that r_{200}^{gals} is in fact a good approximation to r_{200} as determined in this paper from the lensing data to within about 5%. The mass-to-light ratio as a function of radius will be presented in Paper III of this series (Sheldon et al. 2007). Note that N_{200} is dimensionless, and L_{200} has units of $10^{10}h^{-2}L_\odot$.

For the purpose of lensing measurement, the catalog is subdivided into 12 N_{200} richness bins and 16 L_{200} richness bins. The richness boundaries for each richness measure as well as the number of clusters per bin are displayed in Tables 1 and 2.

3. INVERTING CLUSTER PROFILES

3.1. Inversion Method

The methods used to invert the lensing $\Delta\Sigma(R)$ profiles to 3D density and mass profiles are discussed in detail in Johnston et al. (2007) and were first used by
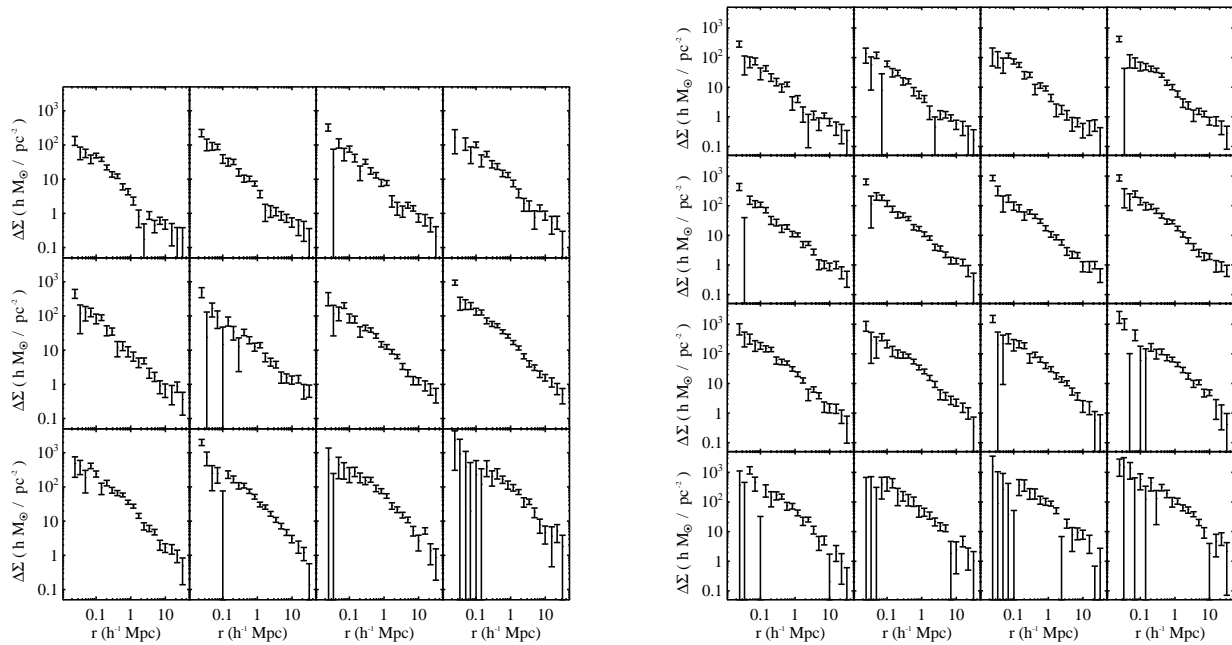
FIG. 1.— **Left:** Weak lensing profiles $\Delta\Sigma(R)$ for 12 bins of optical richness, N_{200}. **Right:** $\Delta\Sigma(R)$ for 16 i-band luminosity bins, L_{200}.

TABLE 2
16 L_{200} BINS

Bin number	$L_{200}(10^{10}h^{-2}L_{\odot})$	Number of clusters per bin
1	5 - 6.24	19618
2	6.24 - 7.8	18597
3	7.8 - 9.74	16042
4	9.74 - 12.2	12269
5	12.2- 15.2	9010
6	15.2 - 19.0	6152
7	19.0 - 23.7	4164
8	23.7 - 29.6	2666
9	29.6 - 36.9	1703
10	36.9 - 46.1	1042
11	46.1 - 57.6	638
12	57.6 - 71.9	344
13	71.9 - 89.8	210
14	89.8 - 112.1	108
15	112.1 - 140	49
16	140 - 450	46

NOTE. — The catalog is also divided into 16 L_{200} richness bins. This table shows the boundaries of L_{200} values and the number of clusters for each bin.

Sheldon et al. (2004) to obtain the galaxy-mass correlation function from galaxy-galaxy lensing measurements. Here, we provide a brief overview of the methods.

The mean excess 3D density profile $\Delta\rho(r)$ around a set of clusters with a given observable O (e.g., richness or luminosity) is best thought of in terms of the cluster–mass two-point correlation function, ξ_{cm}, since $\Delta\rho(r) = \bar{\rho}\,\xi_{cm}(r)$, where $\bar{\rho}$ is the mean density of the Universe. By the assumptions of spatial homogeneity and isotropy, ξ_{cm} depends only on the magnitude of the separation, r, not on direction. As a consequence, the mean density profile $\Delta\rho(r)$ should be very nearly spherically symmetric. Note that this is a purely statistical statement: we do *not* assume that individual cluster density

profiles are spherically symmetric. The spherical symmetry of the average density profile enables the inversion of the stacked lensing signal $\Delta\Sigma(R)$ to the 3D density $\Delta\rho(R)$ and the aperture mass $M(R)$. By contrast, weak lensing measurements of *individual* clusters can only be used to reconstruct the projected 2D mass density, $\Sigma(\vec{x})$, since lensing is produced by all of the mass projected along the line of sight.

The mean 3D density profile is obtained as an integral of the derivative of the shear profile $\Delta\Sigma(R)$ through a purely geometric relation,

$$\Delta\rho(r) = \frac{1}{\pi}\int_r^\infty dR\,\frac{-\Sigma'(R)}{\sqrt{R^2 - r^2}}\ ,\qquad(1)$$

where a prime denotes a derivative with respect to R. The lensing data $\Delta\Sigma$ enters here since it can be shown that

$$-\Sigma'(R) = \Delta\Sigma'(R) + 2\Delta\Sigma(R)/R\ .\qquad(2)$$

The 3D mass profile is given in terms of $\Delta\Sigma(R)$ and $\Delta\rho(R)$ as

$$M(R) = \pi R^2 \Delta\Sigma(R) + 2\pi\int_R^\infty dr\,r\,\Delta\rho(r)\times$$
$$\left[\frac{R^2}{\sqrt{r^2 - R^2}} - 2\left(r - \sqrt{r^2 - R^2}\right)\right].\qquad(3)$$

In practice, these integrals must be truncated at some maximum radius, R_{max}, the largest scale at which one has lensing data ($30h^{-1}$ Mpc for our data). The uncertainty from this truncation is related to the mass-sheet degeneracy. Due to the steepness of the cluster profiles we infer in this paper, this truncation creates only a few percent uncertainty in the last few radial bins of both density or mass and virtually none in bins at smaller radii. Complete details of the procedure are given in Johnston et al. (2007).

3.2. 3D Density and Mass Profiles

The inverted 3D density profiles for each of the 12 N_{200} richness and 16 L_{200} luminosity bins are presented in Figure 2. These profiles are noisier than the shear profiles, since they involve derivatives of noisy data. The differentiation in Eqn. 1 also leads to anti-correlations between neighboring radial bins of $\Delta\rho(r)$.

Figure 3 shows the inverted mean aperture mass profiles, $M(r)$, for the same richness and luminosity bins as above. Since the mass profile is an integral of the density profile, it is smoother than the latter, and neighboring bins of $M(r)$ are statistically correlated. This allows one to better see the deviations from power-law behavior that one expects from the halo model (see §4).

3.3. Direct Measurements of r_{200} and M_{200}

The radius r_{200} is defined, herein, as the radius within which the average density is 200 times the critical density ρ_c. This defines the corresponding mass scale,

$$M_{200} \equiv M(r_{200}) = 200 \; \rho_c(z) \; \frac{4}{3} \; \pi \; r_{200}^3 \; , \qquad (4)$$

where $\rho_c(z) = 3H^2(z)/(8\pi G)$ is the critical density at epoch z, and the Hubble parameter satisfies $H^2(z) = H_0^2 \left[\Omega_m(1+z)^3 + (1-\Omega_m) \right]$ for a flat LCDM Universe. Throughout this paper we use $z = 0.25$, the mean cluster redshift for our sample, and $\Omega_m = 0.27$ to compute $\rho_c(z)$. For these choices, the conversion between M_{200} and r_{200} is $M_{200} = 2.923 \times 10^{14} \; h^{-1}M_\odot \; \left(r_{200}/h^{-1}\mathrm{Mpc}\right)^3$.

Using the inverted mass profiles shown in Fig. 3, we can determine r_{200} and M_{200} in a model independent way, by simply measuring where the curve $200 \; \rho_c(z) \; 4/3 \; \pi \; r^3$ crosses the mass profile. This procedure, which is illustrated in Fig. 3, requires one to interpolate the data between the two radii closest to the crossing point. This interpolation can in principle be ill-defined if the data are noisy and the profiles non-monotonic, but that never occurs for any of our profiles. We have experimented with a few different ways of interpolating. One can use the unique power law defined by the two neighboring data points or fit a power law to a four-point neighborhood of the crossing. We find that these methods give essentially identical answers; since the four-point method yields slightly lower scatter in the mass–richness relation, we use that method.

While this procedure for inferring r_{200} and M_{200} has the advantage of being model independent, the results *cannot* be interpreted as the virial radii and masses of the corresponding dark halos. The primary reason is that BCGs, which we use to define the center of each cluster for the lensing measurements, are not always positioned at the center of mass of the underlying dark matter halo. This fact, which we observe in our simulations, is not surprising: for this analysis, clusters are the objects identified by the maxBCG algorithm, while dark matter halos are theoretical constructs — the two are not in precise one-to-one correspondence (Cohn et al. 2007; Rozo et al. 2007a). The model-independent profiles of Fig. 3, and the corresponding values of r_{200} and M_{200}, are the "true" mass profiles of clusters centered on their BCGs. However, to estimate dark matter halo profiles and masses, we must adopt a model to describe the data, which we do in the next section. When we do so, we find that the

TABLE 3
DIRECT CLUSTER M_{200}^{cl}-RICHNESS CALIBRATION: N_{200} BINS

$\langle N_{200} \rangle$	M_{200}^{cl} ($10^{12}h^{-1}M_\odot$)	r_{200}^{cl} (h^{-1} Mpc)
3.00	4.26 ± 0.45	0.24 ± 0.01
4.00	5.29 ± 0.65	0.26 ± 0.01
5.00	8.01 ± 1.34	0.30 ± 0.02
6.00	13.15 ± 1.65	0.36 ± 0.01
7.00	9.66 ± 2.28	0.32 ± 0.03
8.00	12.71 ± 3.36	0.35 ± 0.03
9.82	25.53 ± 2.86	0.44 ± 0.02
13.91	42.31 ± 3.42	0.53 ± 0.01
20.78	74.45 ± 7.46	0.63 ± 0.02
31.09	123.22 ± 11.28	0.75 ± 0.02
50.27	199.26 ± 24.81	0.88 ± 0.04
92.18	502.87 ± 87.61	1.20 ± 0.07

NOTE. — The M_{200}^{cl} – richness relation for the N_{200} richness bins. This estimate of M_{200} which we call M_{200}^{cl} is meant to represent the M_{200} of the clusters as opposed to the dark matter halos. It is estimated non-parametrically by determining where the 3D mass profile $M(r)$ cross the line determined by $4/3\pi r^3 \; 200 \; \rho_{crit}(z)$. These masses differ from the parametric masses that include cluster miscentering and other effects.

TABLE 4
DIRECT CLUSTER M_{200}^{cl}-RICHNESS CALIBRATION: L_{200} BINS

$\langle L_{200} \rangle$	M_{200}^{cl} ($10^{12}h^{-1}M_\odot$)	r_{200}^{cl} (h^{-1} Mpc)
5.59	4.59 ± 0.77	0.25 ± 0.01
6.97	5.68 ± 0.81	0.27 ± 0.01
8.69	6.16 ± 0.96	0.28 ± 0.01
10.84	12.86 ± 1.42	0.35 ± 0.01
13.53	11.98 ± 1.80	0.34 ± 0.02
16.89	22.92 ± 2.89	0.43 ± 0.02
21.06	30.94 ± 3.60	0.47 ± 0.02
26.31	41.36 ± 4.51	0.52 ± 0.02
32.89	56.90 ± 7.80	0.58 ± 0.03
40.95	77.67 ± 9.78	0.64 ± 0.03
51.19	99.05 ± 13.49	0.70 ± 0.03
64.08	160.65 ± 22.19	0.82 ± 0.04
79.89	160.16 ± 30.13	0.82 ± 0.05
98.69	182.81 ± 35.58	0.86 ± 0.06
124.59	258.49 ± 53.30	0.96 ± 0.07
184.65	553.76 ± 93.41	1.24 ± 0.07

NOTE. — The M_{200}^{cl} – richness relation for the L_{200} richness bins.

inferred dark matter halo masses are about 50% higher than the model-independent cluster masses. We use the results of those model fits to constrain the halo mass – richness relations and other scaling relations.

We will distinguish these two types of masses by referring to the parametric halo masses as M_{200} and non-parametric cluster masses as M_{200}^{cl}. For completeness, we present these cluster masses in Tables 3 and 4 but we will not use them elsewhere in this work. In another publication, Paper III of this series on cluster mass-to-light ratios (Sheldon et al.), we will refer to these non-parametric M_{200}^{cl} masses.

4. HALO MODEL FITS TO LENSING PROFILES

To proceed, we construct a physical model of the average mass density in clusters that comprises three components: the central BCG, the cluster-scale dark matter
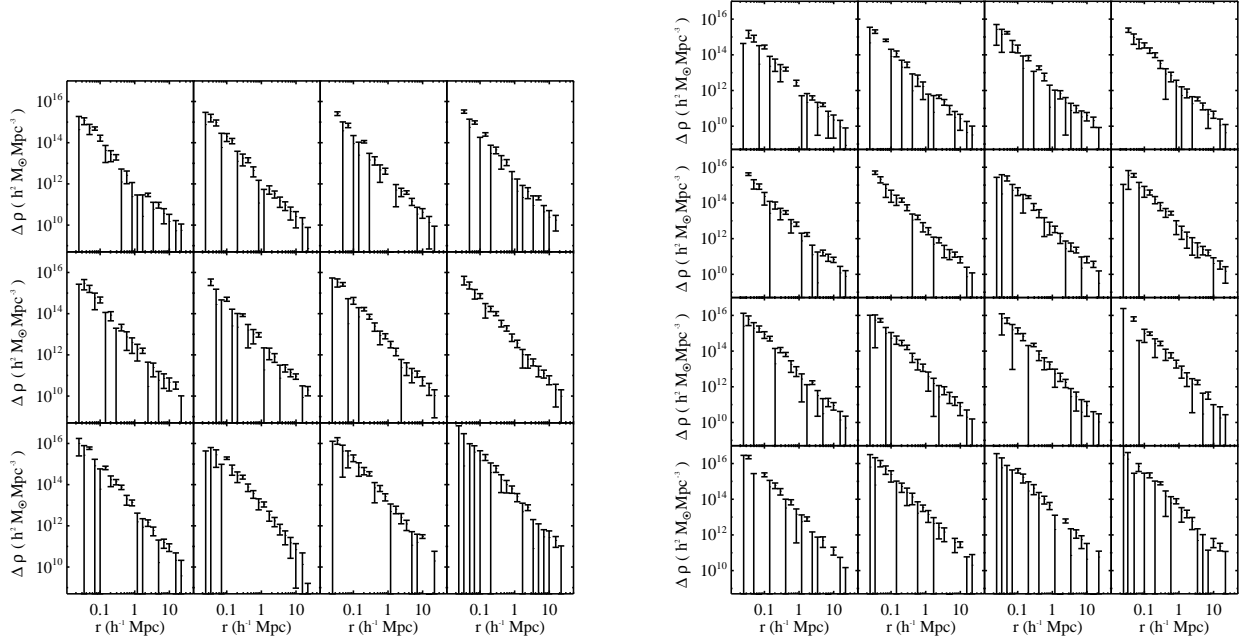
FIG. 2.— **Left:** Inverted mean density profiles, $\Delta\rho(r)$, for the 12 N_{200} richness bins shown in Fig. 1. **Right:** Inverted $\Delta\rho(r)$ profiles for the 16 L_{200} richness bins shown in Fig. 1.
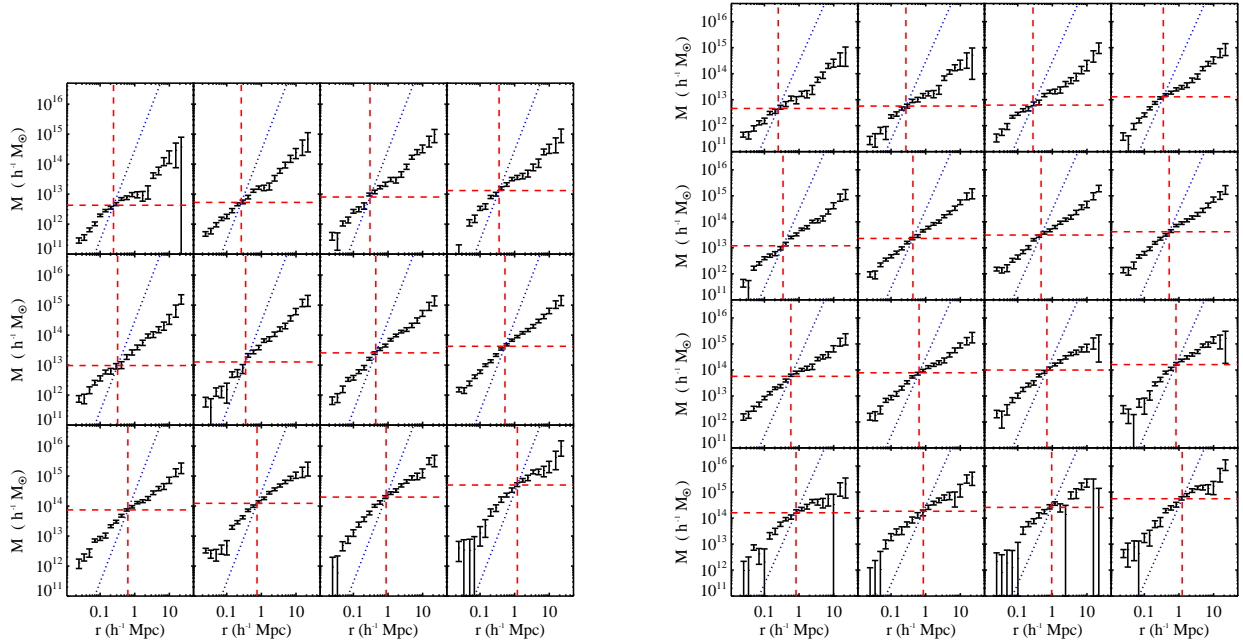

FIG. 3.— **Left:** Inverted 3D aperture mass profiles, $M(r)$, for the 12 N_{200} richness bins. The dotted blue diagonal line in each panel denotes $200\,\rho_c\,4/3\,\pi\,r^3$ (see Eqn. 4); this crosses the mass profile at r_{200} and M_{200}, which are indicated with the dashed red vertical and horizontal lines. **Right:** Inverted 3D aperture mass profiles, $M(r)$, for the 16 L_{200} richness bins.

halo in which it sits, and neighboring mass concentrations. We will also consider non-linear shear. We treat these in turn.

4.1. *The BCG*

Since every maxBCG cluster, by design, is centered on a bright galaxy, we should allow for a contribution to the mass from the baryons (mainly stars) and from the dark matter sub-halo of the BCG (assuming the latter is not modeled by the central cusp of the cluster-scale halo). Gavazzi et al. (2007) find that a central baryonic component is required to fit both the strong and weak lensing profiles of early-type galaxies in the SLACS survey. Although this contribution could be modeled in a number of ways, e.g., by using a de Vaucouleurs profile, its effects are only significant on very small scales, and its form is not well constrained by our data. Therefore, we simply model this contribution as a central point mass, M_0, with lensing signal $\Delta\Sigma = M_0/(\pi R^2)$, where M_0 is a model parameter to be fit.

4.2. *The cluster dark matter halo*

Out to radii of a few Mpc, the density profiles appear to be dominated by the cluster-scale dark matter halos. N-body simulations of structure formation with cold dark matter indicate that halos are reasonably well modeled by the universal (NFW) profiles of Navarro et al. (1997),

$$\rho_{NFW}(r) = \frac{\delta \ \rho_c(z)}{(r/r_s)(1 + r/r_s)^2} \ . \qquad (5)$$

This form contains two free parameters, a scale radius r_s and an amplitude δ; $\rho_c(z)$ is the critical density at redshift z. At $r \sim r_s$, the logarithmic slope of the NFW profile changes between the asymptotic values of -1 at small scales ($r \ll r_s$) and -3 at large scales ($r \gg r_s$). The parameters δ and r_s are usually traded for a description in terms of r_{200} (or equivalently M_{200}) and c_{200}. As above, r_{200} is the radius within which the mean density is 200 times the critical density and for which the enclosed mass is $M(r_{200}) = 200\rho_c(z)(4/3)\pi \ r_{200}^3$, while $c_{200} \equiv r_{200}/r_s$ is the concentration. The amplitude δ can be expressed in terms of c_{200} as

$$\delta = \frac{200}{3} \frac{c_{200}^3}{\ln(1 + c_{200}) - c_{200}/(1 + c_{200})} \ . \qquad (6)$$

Analytic expressions for the shear profile $\Delta\Sigma(R; c_{200}, M_{200})$ of NFW halos can be found in, e.g., Wright & Brainerd (2000). Various other definitions of the virial radius have been used in the literature, e.g., the radius within which the mean density is $180 \ \bar\rho(z)$ instead of $200\rho_c(z)$. We discuss the conversion among these different systems in the Appendix.

4.3. *Miscentering of the BCG and the Halo*

For the lensing measurements, the center of each cluster ($R = 0$) is defined to be the position of the BCG identified by the cluster-finding algorithm. As noted in §3.3, some fraction of the BCGs may be offset from the centers of the corresponding dark matter halos. Such "miscentering" changes the observed tangential shear profile. If the 2D offset in the lens plane is R_s then the azimuthally

averaged $\Sigma(R)$ profile is given by the convolution

$$\Sigma(R|R_s) = \frac{1}{2\pi} \int_0^{2\pi} d\theta \Sigma \left(\sqrt{R^2 + R_s^2 + 2R \ R_s \cos(\theta)} \right) \qquad (7)$$

(Yang et al. 2006).

To make progress, we need to know something about the distribution of offsets, $P(R_s)$. In order to estimate this, we employ N-body simulation-based mock galaxy catalogs that have been constrained to have realistic luminosities, colors, clustering properties, and cluster populations. These catalogs, which have been used in previous maxBCG studies (Koester et al. 2007a; Rozo et al. 2007a,b), populate a dark matter simulation with galaxies using the ADDGALS technique (Wechsler et al 2007). The catalog is based on the light-cone from the Hubble Volume simulation (Evrard et al. 2002), and extends from $0 < z < 0.34$. Galaxies are assigned directly to dark matter particles in the simulation, with a luminosity-dependent bias scheme that is tuned to match local clustering data. The galaxy luminosities are first assigned in the $^{0.1}r$-band, drawn from the luminosity function of Blanton et al. (2003). The luminosity function is assumed to evolve with $Q = 1.3$ magnitudes per unit redshift. We first constrain the relationship between galaxy luminosity and Lagrangian matter densities on a scale of $\sim M*$, using the luminosity-dependent two-point clustering of SDSS galaxies (Zehavi et al. 2005). For each galaxy, a dark matter particle is then chosen on the basis of this density with some $P(\delta|M_r)$. Each mock galaxy is then assigned to a real SDSS galaxy that has approximately the same luminosity and local galaxy density, measured here as the distance to the fifth nearest neighbor. The color for each mock is then given by the SED of this matched galaxy transformed to the appropriate redshift. Because BCGs are now known to be distinct from the general galaxy population, BCG properties are further tuned to match the luminosities and colors of observed BCGs; in addition a BCG is placed at the center of each dark matter halo. This procedure produces a catalog which matches several statistics of the observed SDSS population, including the location, width and evolution of the ridgeline, which makes it ideal for testing the maxBCG algorithm. In this work, we use five galaxy realizations that have been run using the same underlying dark matter simulation; to improve our statistics, we merge all five mock catalogs into one.

The maxBCG algorithm is then used to identify clusters in the mock catalogs, and the resulting BCG positions can be compared to the centers of mass of the dark matter halos in the input N-body simulations. We use the matching technique described in Rozo et al. (2007a) to match clusters to halos, and directly compute the offset R_s between the halo center and the BCG assigned to the halo by the maxBCG cluster finding algorithm. In the real Universe, miscentering for our cluster population can occur for either of two reasons — the real BCG can be offset from the center of mass, or the BCG can be misidenfied by the cluster finder. In the mock catalogs, there is always a bright galaxy at the center of the dark matter halo, so we are neglecting here the first case. Although this is not likely to be precisely true in all cases, our results indicate that miscentering due to misidentified BCGs dominates the effects we discuss

below.

For these catalogs, a richness-dependent fraction of the BCGs appear to be accurately centered on their dark matter halos ($R_s \simeq 0$), while the rest are reasonably well described by a 2D Gaussian distribution,

$$P(R_s) = \frac{R_s}{\sigma_s^2} \exp(-\frac{1}{2}(R_s/\sigma_s)^2) \qquad (8)$$

with $\sigma_s = 0.42 \ h^{-1}$ Mpc, independent of cluster richness (see next section). The resulting mean surface mass profile for the miscentered clusters can be written

$$\Sigma_{NFW}^s(R) = \int dR_s P(R_s) \ \Sigma_{NFW}(R|R_s) \qquad (9)$$

and $\Delta\Sigma_{NFW}^s(R) = \overline{\Sigma^s}_{NFW}(< R) - \overline{\Sigma^s}_{NFW}(R)$. We find that the mean shear profile is not very sensitive to the shape of the distribution of R_s, but it is sensitive to the effective scale length σ_s.

Figure 4 shows the effects of such miscentering on the lensing signal for a cluster with an NFW profile. The effect on $\Delta\Sigma(R)$ is much larger than on $\Sigma(R)$: the convolution in Eqn. 7 leads to a smoothing which essentially flattens the $\Sigma^s(R)$ profile at small scales, creating a mass sheet which causes little shear. While the $\Delta\Sigma_{NFW}(R)$ profile is relatively flat at small scales, the smoothed $\Delta\Sigma_{NFW}^s(R)$ profile is strongly suppressed at scales $R \lesssim 2.5\sigma_s$.

In applying this model to the data in §5, we include $\ln(\sigma_s)$ as a model parameter, using its value from the mock catalogs as the central value of a Gaussian prior probability distribution. We assume that a fraction p_c of the BCGs are accurately centered on the dark matter halos, and that a fraction $1 - p_c$ follow the distribution of Eqn. 8. The simulations are used to formulate a prior distribution for p_c, as described in §4.5.

We determine this fraction p_c of correctly centered BCGs as a function of N_{200}; this is shown in the left panel of Figure 5. We can model this relation as $p_c(N_{200}) \equiv 1/(1 + \exp(-q))$ with

$$q = \ln(1.13 + 0.92 \ (N_{200}/20)). \qquad (10)$$

The dotted lines show the statistical 95% confidence bands recovered in the simulations, whereas the dashed lines show the 95% bands corresponding to the much more generous 0.4 prior on q used in our analysis as described in §4.5. The right panel of Figure 5 shows the miscentering distribution $P(R_s)$. The data from the simulations is roughly fit by a two dimensional Gaussian of width $\sigma_R = 0.42 \ h^{-1}$ Mpc. Note that because the mock catalogs place the BCG of a halo at the center of the halo, the offset R_s is identically zero if maxBCG assigns the correct BCG to each cluster.

Our best fit model is shown as a solid line, while the dashed lines show the models that bound the 68% confidence regions corresponding to the 30% Gaussian prior on the parameter σ_S used in §4.5 to fit the data. It is clear that our adopted priors are much more generous than the statistical noise in the simulations. We choose this wider prior since there may be differences between the mock catalogs and the real data. The wider prior likely can mostly account for real offsets between BCGs and the center of the mass concentration. Finally, we
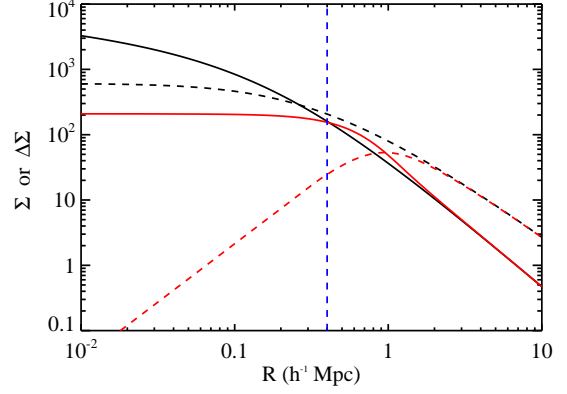

FIG. 4.— Effect of an offset between the BCG and the halo center on the projected mass profile $\Sigma(R)$ and the lensing signal $\Delta\Sigma(R)$. The black solid curve shows the $\Sigma(R)$ profile for an NFW halo with $c_{200} = 5$ and $r_{200} = 1 \ h^{-1}$ Mpc. The black dashed curve shows the corresponding $\Delta\Sigma(R)$ profile. The red curves show the resulting mean profiles when the distribution of randomly-oriented BCG-halo offsets is a 2D Gaussian with dispersion $\sigma_s = 0.42 h^{-1}$ Mpc (indicated by the blue vertical line). The red solid curve shows the smoothed $\Sigma^s(R)$ and the red dashed curve the smoothed $\Delta\Sigma^s(R)$ profile. Miscentering has the effect of making the $\Sigma^s(R)$ nearly flat, i.e., a mass sheet, at small scales. Although $\Sigma(R)$ and $\Sigma^s(R)$ differ by only $10-30\%$ near $r = \sigma_s$, $\Delta\Sigma$ and $\Delta\Sigma^s$ differ by an order of magnitude. For this example, $\Delta\Sigma^s(R)$ peaks at $r \simeq 2.5\sigma_s$; this behavior depends slightly on c_{200}.

emphasize here that we are adopting the same miscentering distribution for all richness bins. The differences between the various richness bins in the mock data are much smaller than the 30% prior that we use.

4.4. Neighboring mass concentrations

The NFW profile is expected to be a good representation of the stacked mass profiles on small to intermediate scales surrounding clusters, but on large scales the lensing signal is dominated by neighboring mass concentrations, e.g., nearby halos and filaments. We model this contribution via the so-called two-halo term (Seljak 2000; Mandelbaum et al. 2005),

$$\rho_{2h}(r) = b(M_{200}, z) \ \Omega_m \ \rho_{c,0} \ (1 + z)^3 \ \xi_l(r, z) \qquad (11)$$

where $\rho_{c,0}$ is the critical density at the present epoch, and $\xi_l(r, z)$ is the auto-correlation function of the mass in linear perturbation theory, evaluated at the redshift of the clusters. Here, $b(M_{200}, z)$ is the linear bias parameter for dark matter halos, which has a predicted dependence upon halo mass and redshift (Sheth & Tormen 1999; Seljak & Warren 2004b).

The shape of the linear correlation function is determined by the cosmological parameters n_s, h, and Ω_m for a flat LCDM model and is constrained by observations of galaxy clustering (Eisenstein et al. 2005; Zehavi et al. 2004). The linear correlation function can be expressed as

$$\xi_l(r, z) = D(z)^2 \ \sigma_8^2 \ \xi_l((1 + z) \ r) , \qquad (12)$$

where $\xi_l(r)$ with a single argument is the linear correlation function evaluated at $z = 0$ and normalized to $\sigma_8 = 1$. The presence of the factor of $(1 + z)$ in the above
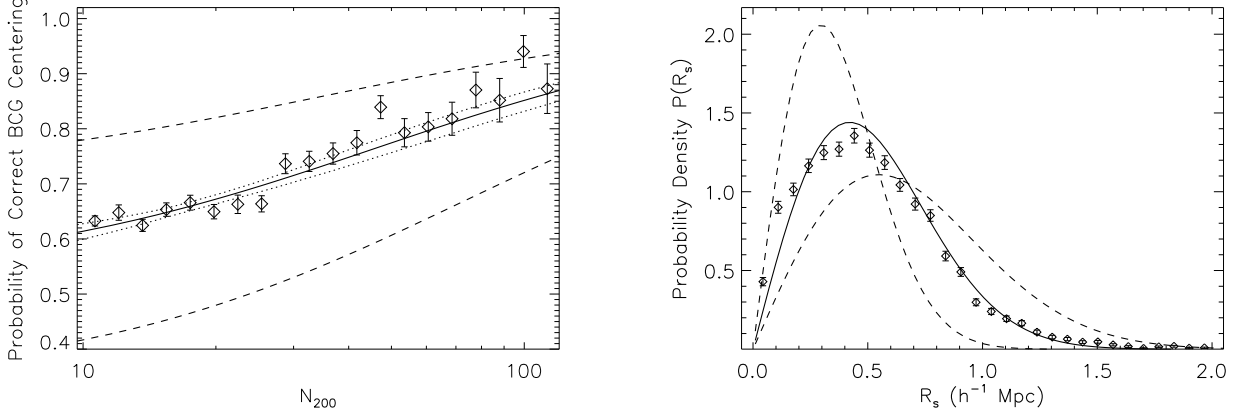
FIG. 5.— **Left:** The probability that a cluster is correctly centered as a function of cluster richness, N_{200}, in mock catalogs. The diamonds with error bars are the measurements in the simulations, whereas the solid line is our best fit model (see text for details). The dotted lines show the 95% confidence (2σ) band from statistical uncertainties only. The dashed line shows the more generous 95% confidence region corresponding to the adopted 0.40 prior uncertainty on q, which are wider to allow for some possibility that there are differences in the probability of a cluster being correctly centered between our mocks and the real data. **Right:** The distribution of the projected radial offsets between a halos and clusters which are not correctly centered. Diamonds with error bars show the measurement in the mocks, while the solid line represents the best 2D Gaussian model, corresponding to a width $\sigma_S = 0.42 \ h^{-1}$ Mpc. The dashed lines are the two models that bound the much more generous 68% confidence region of σ_S with the adopted 30% prior on σ_S.

expression converts the *physical* distance r into *comoving* units. All distances in this paper are in *physical* not *comoving* units. The linear growth factor satisfies

$$D(a) \propto H(a) \int da' \, [H(a')a']^{-3} \, , \qquad (13)$$

with $a = 1/(1+z)$; D is normalized to unity at $a = 1$ ($z = 0$). We can therefore express the two-halo contribution to the density as

$$\rho_{2h}(r) = B\rho_{c,0} \, (1+z)^3 \, \xi_l((1+z) \, r) \, , \qquad (14)$$

where we have defined an effective bias parameter

$$B \equiv b(M_{200}, z) \, \Omega_m \, \sigma_8^2 \, D(z)^2 \, . \qquad (15)$$

The contribution of the two-halo term to the lensing signal, for fixed values of n_s, h, and Ω_m, can be written as $\Delta\Sigma(R; B) = B\Delta\Sigma_l$, where, as before, $\Delta\Sigma_l(R) = \overline{\Sigma}_l(<R) - \overline{\Sigma}_l(R)$, and

$$\Sigma_l(R) = (1+z)^3\rho_{c,0} \int dy\xi_l \left((1+z)\sqrt{y^2 + R^2}\right)$$

$$= (1+z)^2\rho_{c,0} \, W \, ((1+z)R) \qquad (16)$$

with

$$W(R) \equiv \int dy \, \xi_l(\sqrt{y^2 + R^2}) \, . \qquad (17)$$

4.5. *Summary of halo model and parameter priors for* $\Delta\Sigma$ *fits*

Combining the results from sections 4.1 through 4.4, we can write down the model for the lensing signal $\Delta\Sigma$ thus far,

$$\Delta\Sigma(R) =$$
$$\frac{M_0}{\pi R^2} + p_c\Delta\Sigma_{NFW}(R) + (1 - p_c)\Delta\Sigma_{NFW}^s(R) + B\Delta\Sigma_l$$
$$(18)$$

where, sequentially, the terms come from the BCGs, the halos centered on the BCGs, the halos not centered on the BCGs, and the neighboring halos.

There are two further effects to consider. This model assumes a constant halo mass where, in reality, the signal will be averaged over the distribution of halos masses for each richness bin. The other effect that we will consider is the non-linear shear effect that is discussed in Mandelbaum et al. (2006). We will treat this non-linear contribution first and then integrate the full signal over the distribution of masses.

The average tangential ellipticities do not trace the shear exactly but rather trace the *reduced shear*, $g \equiv \gamma/(1 - \kappa)$. Let e_{ij} be the i-th source galaxy around cluster j for some radial bin. As shown in Mandelbaum et al. (2006) an estimator for $\Delta\Sigma$ formed from a weighted average of ellipticities and identical halos has a second order contribution

$$\widehat{\Delta\Sigma} = \sum_{ij} W_{ij} \, e_{ij}$$
$$= \Delta\Sigma + \Delta\Sigma \, \Sigma \, \mathcal{L}_Z \qquad (19)$$

with

$$\mathcal{L}_Z = \left\langle \Sigma_{crit}^{-3} \right\rangle / \left\langle \Sigma_{crit}^{-2} \right\rangle \qquad (20)$$

This differs from the $\left\langle \Sigma_{crit}^{-2} \right\rangle / \left\langle \Sigma_{crit}^{-1} \right\rangle$ in Mandelbaum et al. (2006) in that our weighting has an explicit factor of Σ_{crit}^{-1}.

$$W_{ij} = \frac{1}{2R} \frac{\sigma_{ij}^{-2}\Sigma_{crit}^{-1}(i, j)}{\sum_{kl} \sigma_{kl}^{-2}\Sigma_{crit}^{-2}(k, l)} \qquad (21)$$

where R is the shear responsivity and σ_{kl}^2 are the estimates of variances on source ellipticities.

Using the photometric redshifts for the source galaxies and the maxBCG photometric estimates for the cluster redshifts, we find $\mathcal{L}_Z = 1.40 \times 10^{-4} \ h^{-1} \ \mathrm{pc}^2/M_\odot$. This quantity varies only a few percent across different cluster samples and different radial bins; a variation we ignore.

For the last step we need to consider that within any richness bin, there will be scatter in mass. So we need to integrate this expression over the probability distribution of halos masses $P(M_{200})$. Here, $\langle \ \rangle$ indicates averaging over $P(M_{200})$.

$$\widehat{\langle \Delta\Sigma \rangle} = \langle \Delta\Sigma \rangle + \langle \Delta\Sigma \ \Sigma \rangle \ \mathcal{L}_Z \qquad (22)$$

We will use a log-normal distribution of M_{200} at fixed richness with a variance in $\ln M_{200}$ given by V_M which is our last model parameter.

For the first term $\langle \Delta\Sigma \rangle$ we can integrate Eqn. 18 over $P(M_{200})$. Corresponding to Eqn. 18, there is a three-term expression for Σ (the point-mass doesn't contribute). So our second order correction has 12 terms that need to be integrated over $P(M_{200})$. Most of these pairs (i, j) do not contribute since $\langle \Delta\Sigma_i \ \Sigma_j \rangle (R) \ \mathcal{L}_Z \ll \langle \Delta\Sigma \rangle (R)$ at all scales.

Only two of these terms make meaningful contributions at the smallest scales,

$$\Delta\Sigma_{NL} = \mathcal{L}_Z \times$$
$$\left[p_c^2 \langle \Delta\Sigma_{NFW} \ \Sigma_{NFW} \rangle + \frac{p_c M_0}{\pi R^2} \langle \Sigma_{NFW} \rangle \right]. \qquad (23)$$

With this last expression we can write down our full model for our data where, again, $\langle \ \rangle$ indicates averaging over $P(M_{200})$.

$$< \widehat{\Delta\Sigma(R)} > =$$
$$\frac{M_0}{\pi R^2} + p_c \langle \Delta\Sigma_{NFW} \rangle (R)$$
$$(1 - p_c) \langle \Delta\Sigma_{NFW}^s \rangle (R) + B\Delta\Sigma_l + \Delta\Sigma_{NL}$$
$$\qquad (24)$$

This model has seven parameters: the BCG point mass M_0; the two NFW halo parameters r_{200} and c_{200}; the scatter in the mass–richness relation V_M; the halo mis-centering width σ_s and the halo centering fraction p_c; the linear bias amplitude $B = b(M_{200})\Omega_m\sigma_8^2 D^2(z)$ which should also be thought of as the *average* over the mass distribution.

Since we will integrate over $P(M_{200})$ we need to be specific about what we mean by our parameter r_{200}. We take this to be the r_{200} corresponding to the *average* M_{200}. For a log-normal distribution $< M_{200} >= \exp(V_M/2+\mu)$ where μ is the average $\ln(M_{200})$.

Becker et al. (2007) measures the variance of the logarithm of the galaxy velocity dispersion as $Var(\sigma_v) = 0.0963 - 0.0241(N_{200}/25)$ and Evrard et al. (2007) determines the scaling $M_{200} \propto \sigma_v^\lambda$ with $\lambda = 2.98$. This results in

$$V_M = 0.855 - 0.214 \ln(N_{200}/25). \qquad (25)$$

We allow for an uncertainty of 0.60 in V_M in our prior (i.e. a 30% uncertainty for the scatter). This log-normal model also seems consistent with our mock catalogs.

Table 5 lists all seven model parameters used in the fits, including the information about the prior distributions. To enforce positivity, logarithms are used for all parameters except B and M_0. Each prior distribution is taken to be a Gaussian with mean and standard deviation as indicated in the table. In addition M_0 is forced to

be positive since it is not at all constrained on the lower end. Here, a "weak prior" means that neither the best-fit parameters nor the estimated parameter errors change significantly if the standard deviation of the prior distribution is increased. Since the parameter p_c is constrained to lie in the range $[0, 1]$, we use the transformed parameter $q \equiv \ln[p_c/(1 - p_c)]$ which has range $[-\infty, +\infty]$ and can thus be assigned a Gaussian prior. The prior mean of q and V_M vary with richness as described in Eqn. 10 and 25.

To fit the measured $\Delta\Sigma$ profiles with the model, we use a Markov Chain Monte Carlo (MCMC). MCMC is useful for efficiently calculating likelihoods in multi-dimensional parameter spaces. MCMC methods generate "chains" or sequences in the parameter space that represent a fair sampling from the full posterior probability distribution. Thus, they allow one to visualize the likelihood surface and see degeneracies between parameters without assuming that the errors are normally distributed (as in the Fisher matrix method). It is also straightforward to include priors on parameters in the MCMC approach. Our MCMC routine uses the Metropolis-Hastings algorithm with Gaussian transition functions. The total number of steps is 100,000, and we discard a burn-in period of the first 1000 steps. Runs of varying length show that convergence of the posterior distribution is reached before 10,000 steps and longer runs such as our 100,000 step run improve the sampling but do not affect the sample mean or variances by meaningful amounts.

4.6. Systematic errors

There are two major sources of systematic error in any weak lensing measurements: shear calibration error and errors associated with photo-z biases. The shear calibration error of the shear estimation methods that we use for the SDSS were tested as part of the Shear TEsting Program II (STEP2 ; Massey et al. (2007)) and found to be less than a percent (for the RM method in STEP2). However, we allow for a 3% error in shear calibration since the STEP simulation error may not represent the full calibration error when these methods are applied to real data — e.g., the PSF modeling of SDSS was not tested in STEP.

The dominant systematic error is that associated with biases in the photometric redshift distribution. We use a neural network based method (Cunha et al. In preparation) which uses a training set of spectroscopic redshifts from the SDSS, CNOC2 (Yee et al. 2001) and CFRS (Lilly et al. 1995). See Paper I for details.

Although it is difficult to estimate the residual photo-z bias, we will assume that the amplitude of the resultant masses is uncertain at the level of 7% and we will include this in our errors of the zero-point of the mass–richness relation. Further improvements in photo-z calibration should be able to reduce this overall error by as much as a few percent.

Another source of systematic errors is model dependency. The priors that we have chosen are considered to be independent between richness bins and so combining 12 to 16 bins of data reduces the effective width of these priors by about 4 when considering averaged quantities such as the mass–richness relation (see §5.1). However if the prior means for these quantities such as q and V_M are shifted *systematically* from their true values, the effect of

Param #	Parameter	Description	Prior-mean	Prior-sigma	Note
1	$\ln(r_{200})$	r_{200} radius	-0.693	1.5	weak prior
2	$\ln(c_{200})$	concentration	1.386	3	weak prior
3	B	bias amplitude	0.5	4.0	weak prior
4	q	miscentering parameter	see text	0.4	strong prior
5	$\ln(\sigma_S)$	miscentering width	-0.868	0.3	strong prior
6	M_0	point mass ($10^{12}\ h^{-1}M_\odot$)	0	2.5	weak prior
7	V_M	variance of $\ln(M_{200})$	see text	0.6	strong prior

NOTE. — Parameters in the model (Eqn. 24) for $\Delta\Sigma$. The mean and standard deviation for the Gaussian prior distribution are given as well as a brief description.

these maginalizations may not fully account for this. By experimenting with different values for these prior means we can estimate the possible level of additional systematic errors. For the mass–richness relation we estimate that this will contribute an additional systematic error of 10%. The concentration, c_{200}, is more affected by shifts in these nuisance parameters, particularly q and M_0. We allow for a 30% systematic error on the amplitude of the c_{200}–M_{200} relation §5.2. The bias parameter, B is less affected by these nuisance parameters but as we shall see in §5.3, some knowledge of V_M is required to compare it with theoretical predictions.

5. RESULTS OF HALO MODEL FITS

Figure 6 shows the result of an MCMC run for the seventh M_{200} richness bin. These are the one-dimensional marginal posteriors for the 7 parameters. Most resemble a normal distribution with the exception of M_0 which is constrained to be strictly positive. The red lines indicate the prior normal distribution for each. The first three $\ln R_{200}$, $\ln c_{200}$ and B have uninformative priors whereas q, $\ln \sigma_S$ and $\ln V_M$ have constraining priors. That is, in the later case, the posterior resembles the prior; the data are uninformative for these three.

Figure 7 shows the marginal posterior distributions for all 21 pairs of parameters for the same bin. The red region is the 68% (1 σ) confidence region; green is the 95% (2 σ) confidence region and blue is the 99% (3 σ) confidence region. Although none of these parameters appear to be strongly degenerate at these noise levels, there is some correlation. R_{200} is correlated with both q and V_M and c_{200} is correlated with q and M_0. These contours also allow for an estimate of how the best fit parameters might be biased if we have systematically misestimated our nuisance parameter priors. If the shot noise were significantly smaller, these correlations with nuisance parameters would become more dominant sources of error, and so modeling the effect of these (and possibly other) parameters will become a more critical issue for future experiments.

The results of fitting this model to the $\Delta\Sigma$ profiles in the 12 N_{200} richness and 16 L_{200} luminosity bins are shown in Figures 8 and 9. In each panel, the green curve shows the NFW halo profile, the blue curve indicates the two-halo term, the red curve is the BCG point mass term, the orange curve is the smoothed (miscentered) NFW halo component, and the purple dashed curve shows the non-linear correction. The magenta curve shows the sum of these terms. One can see that the model does a good job of fitting all of the features in the shear profiles, the

most prominent of which is the one-halo to two-halo transition, which usually occurs near r_{200}. The best fit parameters for r_{200}, c_{200} and B, properly marginalized over the nuisance parameters, are shown in Tables 6 and 7. We show the values for mass and concentration converted to other mass definitions in Tables 8 and 9. The method of conversion is discussed in the Appendix.

Figure 10 shows the best-fit models over-plotted on the inverted 3D mass profiles that were previously shown in Figure 3. Because the mass profiles are less noisy, they more clearly display the features in the data. The one-halo to two-halo transition is most prominent in the lowest richness and luminosity bins.

5.1. *The mass–richness relation*

Figure 11 shows the inferred central halo mass–richness relations for both N_{200} and L_{200} richness measures. The red line in each case shows the resulting power-law fit to the relation. The fit to the mass–richness relation is

$$M_{200}(N_{200}) = M_{200|20}(N_{200}/20)^{\alpha_N} \qquad (26)$$

with

$$M_{200|20} = (8.8 \pm 0.4_{stat} \pm 1.1_{sys}) \times 10^{13}h^{-1}M_\odot$$
$$\alpha_N = 1.28 \pm 0.04.$$

The mass–luminosity relation is found to be

$$M_{200}(L_{200}) = L_{200|40}(L_{200}/40)^{\alpha_L} \qquad (27)$$

with

$$M_{200|40} = (9.5 \pm 0.4_{stat} \pm 1.2_{sys}) \times 10^{13}h^{-1}M_\odot$$
$$\alpha_L = 1.22 \pm 0.04.$$

The statistical error on the zero-point of both mass richness relations is about 5%. This includes the full marginalization over the other six model parameters. As discussed in §4.6 we need to include systematic errors due to shear calibration and possible photo-z biases as well as any remaining systematic biases in our modeling. We allow for a 3% shear calibration bias, a 7% photo-z bias and 10% for modeling biases. so this increases the error on the zero-point of the mass–richness relations to about 13%.

To accommodate other conventions used in the literature, power-law fits to the mass and concentration data for for alternate mass-scale definitions (see Tables 8 and 9) are shown in Tables 10 and 11.

While this seven-parameter model may appear overly complicated, it is necessary in order to properly account for the full uncertainty in modeling the cluster shear profiles. For example, if we were to ignore miscentering
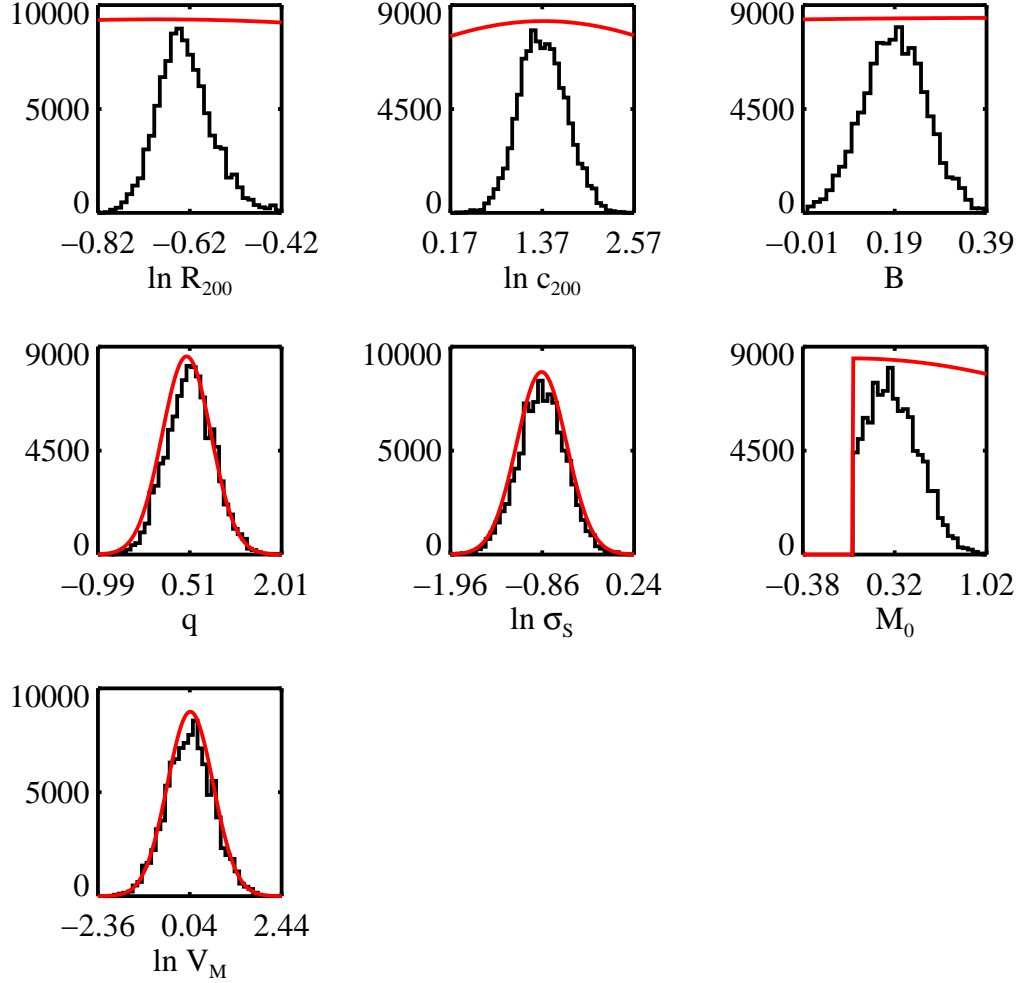
FIG. 6.— This shows the one-dimensional marginal posteriors for the 7 parameters for the seventh N_{200} richness bin. Most resemble a normal distribution The red lines indicate the prior normal distribution for each (with arbitrary normalization). The first three $\ln R_{200}$, $\ln c_{200}$ and B have uninformative priors whereas q, $\ln \sigma_S$ and $\ln V_M$ have constraining priors; i.e. the posterior resembles the prior so the data are uninformative for these. The prior for M_0 is constrained to be positive but is largely uninformative beyond that.

TABLE 6
BEST FIT PARAMETERS: N_{200} BINS

$< N_{200} >$	M_{200} ($10^{12} h^{-1} M_\odot$)	r_{200} (h^{-1} Mpc)	c_{200}	B
3.00	6.37 ± 1.04	0.28 ± 0.015	5.78 ± 1.35	0.07 ± 0.03
4.00	9.77 ± 1.80	0.32 ± 0.020	6.17 ± 2.29	0.11 ± 0.04
5.00	14.63 ± 2.90	0.37 ± 0.024	4.45 ± 1.58	0.17 ± 0.05
6.00	21.35 ± 3.66	0.42 ± 0.024	4.33 ± 1.12	0.13 ± 0.06
7.00	23.31 ± 5.56	0.43 ± 0.034	5.77 ± 2.35	0.18 ± 0.07
8.00	27.86 ± 6.97	0.46 ± 0.038	2.34 ± 1.01	0.25 ± 0.09
9.82	44.14 ± 7.96	0.53 ± 0.032	3.97 ± 1.21	0.19 ± 0.07
13.91	60.01 ± 8.45	0.59 ± 0.028	4.22 ± 1.12	0.23 ± 0.08
20.78	95.96 ± 12.58	0.69 ± 0.030	5.82 ± 1.49	0.25 ± 0.10
31.09	167.76 ± 23.39	0.83 ± 0.039	2.95 ± 0.66	0.24 ± 0.13
50.27	252.06 ± 35.28	0.95 ± 0.044	4.01 ± 0.86	0.46 ± 0.20
92.18	568.81 ± 87.75	1.25 ± 0.064	2.92 ± 0.76	0.48 ± 0.36

NOTE. — This shows the best fit parameters of interest from the MCMC for the N_{200} richness bins. We have marginalized over the four nuisance parameters.
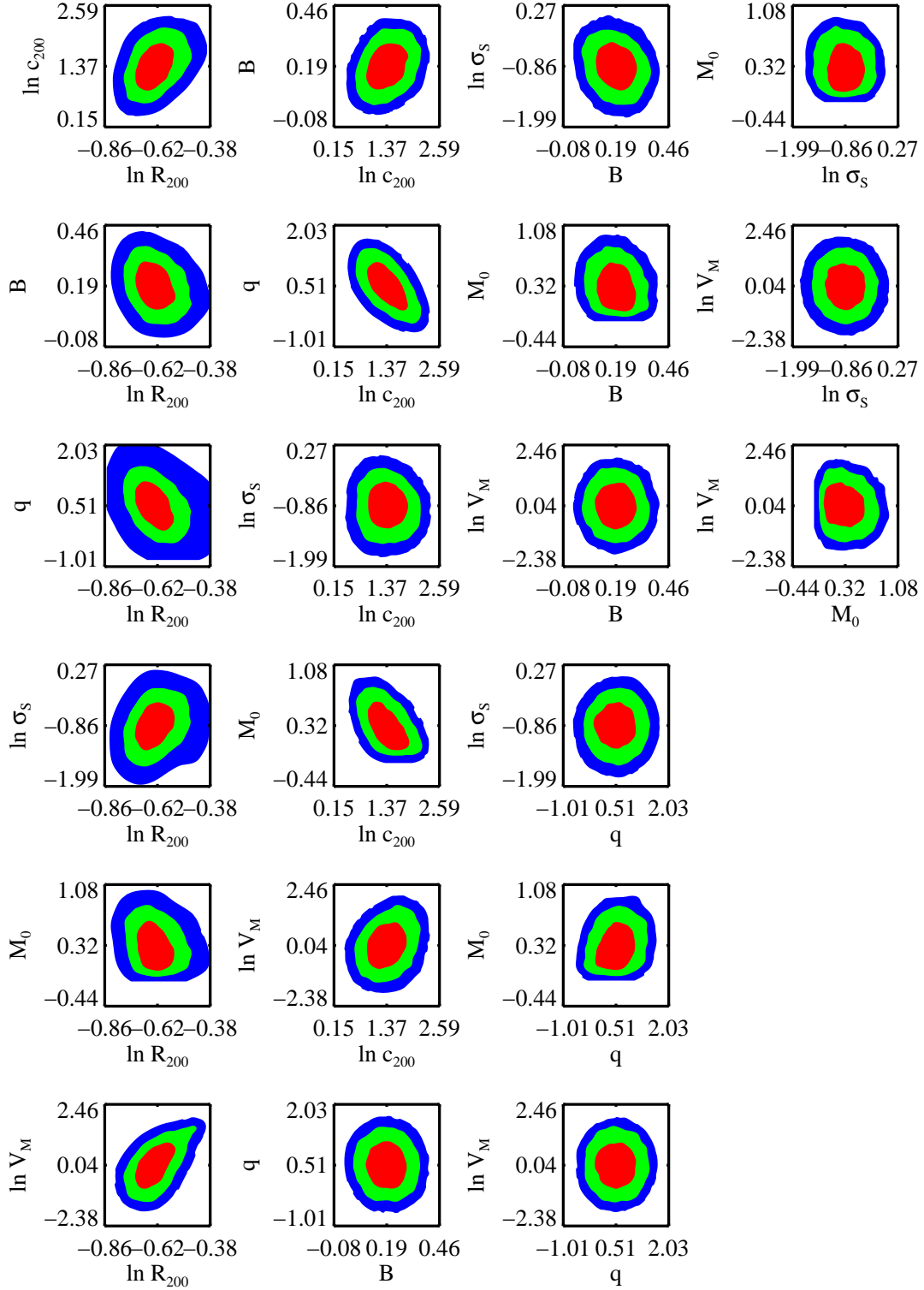
FIG. 7.— The results of the MCMC chain for the seventh N_{200} richness bin. This shows the marginal posterior distributions for all 21 pairs of parameters. The red region is the 68% (1 σ) confidence region; green is the 95% (2 σ) confidence region and blue is the 99% (3 σ) confidence region. Although none of these parameters appear to be strongly degenerate at these noise levels, there is some correlation. R_{200} is correlated with both q and V_M and c_{200} is correlated with q and M_0. These contours also allow for an estimate of how the best fit parameters might be biased if we have systematically misestimated our nuisance parameter priors.

TABLE 7
Best Fit Parameters: L_{200} Bins

$< L_{200} >$	M_{200} ($10^{12}h^{-1}M_\odot$)	r_{200} (h^{-1} Mpc)	c_{200}	B
5.59	7.87 ± 1.84	0.30 ± 0.023	5.31 ± 2.39	0.14 ± 0.04
6.97	9.19 ± 1.91	0.32 ± 0.022	5.21 ± 1.79	0.13 ± 0.04
8.69	13.62 ± 2.45	0.36 ± 0.022	6.86 ± 1.88	0.08 ± 0.04
10.84	18.23 ± 3.22	0.40 ± 0.023	4.20 ± 1.20	0.14 ± 0.05
13.53	29.65 ± 5.99	0.47 ± 0.031	4.77 ± 1.73	0.16 ± 0.06
16.89	37.44 ± 6.36	0.50 ± 0.029	5.20 ± 1.70	0.24 ± 0.07
21.06	41.79 ± 7.27	0.52 ± 0.030	3.88 ± 1.19	0.22 ± 0.07
26.31	59.58 ± 9.34	0.59 ± 0.031	4.99 ± 1.47	0.28 ± 0.09
32.89	78.32 ± 11.88	0.64 ± 0.033	6.01 ± 1.62	0.24 ± 0.10
40.95	97.25 ± 14.51	0.69 ± 0.034	5.41 ± 1.47	0.28 ± 0.11
51.19	141.43 ± 23.27	0.79 ± 0.043	4.16 ± 1.22	0.21 ± 0.12
64.08	204.05 ± 33.23	0.89 ± 0.048	2.67 ± 0.75	0.30 ± 0.18
79.89	210.75 ± 35.03	0.90 ± 0.050	4.09 ± 1.13	0.16 ± 0.12
98.69	235.24 ± 47.69	0.93 ± 0.063	4.11 ± 1.41	0.48 ± 0.27
124.59	327.90 ± 62.23	1.04 ± 0.066	3.75 ± 1.13	0.47 ± 0.31
184.65	610.42 ± 99.89	1.28 ± 0.070	3.45 ± 0.90	0.39 ± 0.31

NOTE. — This shows the best fit parameters of interest from the MCMC for the L_{200} richness bins.We have marginalized over the four nuisance parameters.

TABLE 8
Mass Richness: N_{200} Bins

$< N_{200} >$	M_{200}	c_{200}	M_{180b}	c_{180b}	M_{vir}	c_{vir}	M_{500}	c_{500}
3.00	6.37	5.78	8.27	8.72	7.41	7.26	4.72	3.85
4.00	9.77	6.17	12.58	9.28	11.30	7.74	7.31	4.12
5.00	14.63	4.45	19.66	6.80	17.35	5.64	10.34	2.92
6.00	21.35	4.33	28.82	6.63	25.39	5.49	15.01	2.84
7.00	23.31	5.77	30.25	8.71	27.08	7.25	17.24	3.84
8.00	27.86	2.34	42.04	3.71	35.40	3.03	16.89	1.46
9.82	44.14	3.97	60.39	6.09	52.91	5.04	30.49	2.58
13.91	60.01	4.22	81.34	6.45	71.54	5.35	41.97	2.76
20.78	95.96	5.82	124.42	8.78	111.44	7.31	71.09	3.88
31.09	167.76	2.95	241.65	4.60	207.35	3.78	108.26	1.88
50.27	252.06	4.01	344.24	6.16	301.85	5.10	174.52	2.62
92.18	568.81	2.92	820.81	4.56	703.78	3.75	366.17	1.86

NOTE. — Maximum likelihood mean halo mass and concentration parameters for each richness bin converted from our $200\rho_c$ definition of virial mass into three other common definitions. The unit of mass is $10^{12}h^{-1}M_\odot$.

TABLE 9
Mass Richness: L_{200} Bins

$< L_{200} >$	M_{200}	c_{200}	M_{180b}	c_{180b}	M_{vir}	c_{vir}	M_{500}	c_{500}
5.59	7.87	5.31	10.32	8.04	9.20	6.69	5.74	3.52
6.97	9.19	5.21	12.09	7.89	10.76	6.56	6.68	3.45
8.69	13.62	6.86	17.32	10.29	15.63	8.59	10.34	4.61
10.84	18.23	4.20	24.72	6.43	21.74	5.32	12.74	2.74
13.53	29.65	4.77	39.47	7.26	34.98	6.03	21.23	3.14
16.89	37.44	5.20	49.25	7.88	43.85	6.55	27.22	3.44
21.06	41.79	3.88	57.37	5.97	50.20	4.93	28.73	2.52
26.31	59.58	4.99	78.81	7.58	70.01	6.30	43.00	3.30
32.89	78.32	6.01	101.14	9.06	90.74	7.55	58.32	4.01
40.95	97.25	5.41	127.27	8.18	113.56	6.81	71.18	3.59
51.19	141.43	4.16	192.06	6.38	168.80	5.28	98.64	2.72
64.08	204.05	2.67	299.66	4.19	255.11	3.44	128.33	1.68
79.89	210.75	4.09	286.93	6.28	251.92	5.19	146.50	2.67
98.69	235.24	4.11	320.05	6.30	281.08	5.22	163.68	2.68
124.59	327.90	3.75	452.69	5.78	395.19	4.77	223.80	2.43
184.65	610.42	3.45	854.38	5.35	741.71	4.41	409.17	2.23

NOTE. — Maximum likelihood mean halo mass and concentration parameters for each luminosity bin converted from our $200\rho_c$ definition of virial mass into three other common definitions. The unit of mass is $10^{12}h^{-1}M_\odot$.
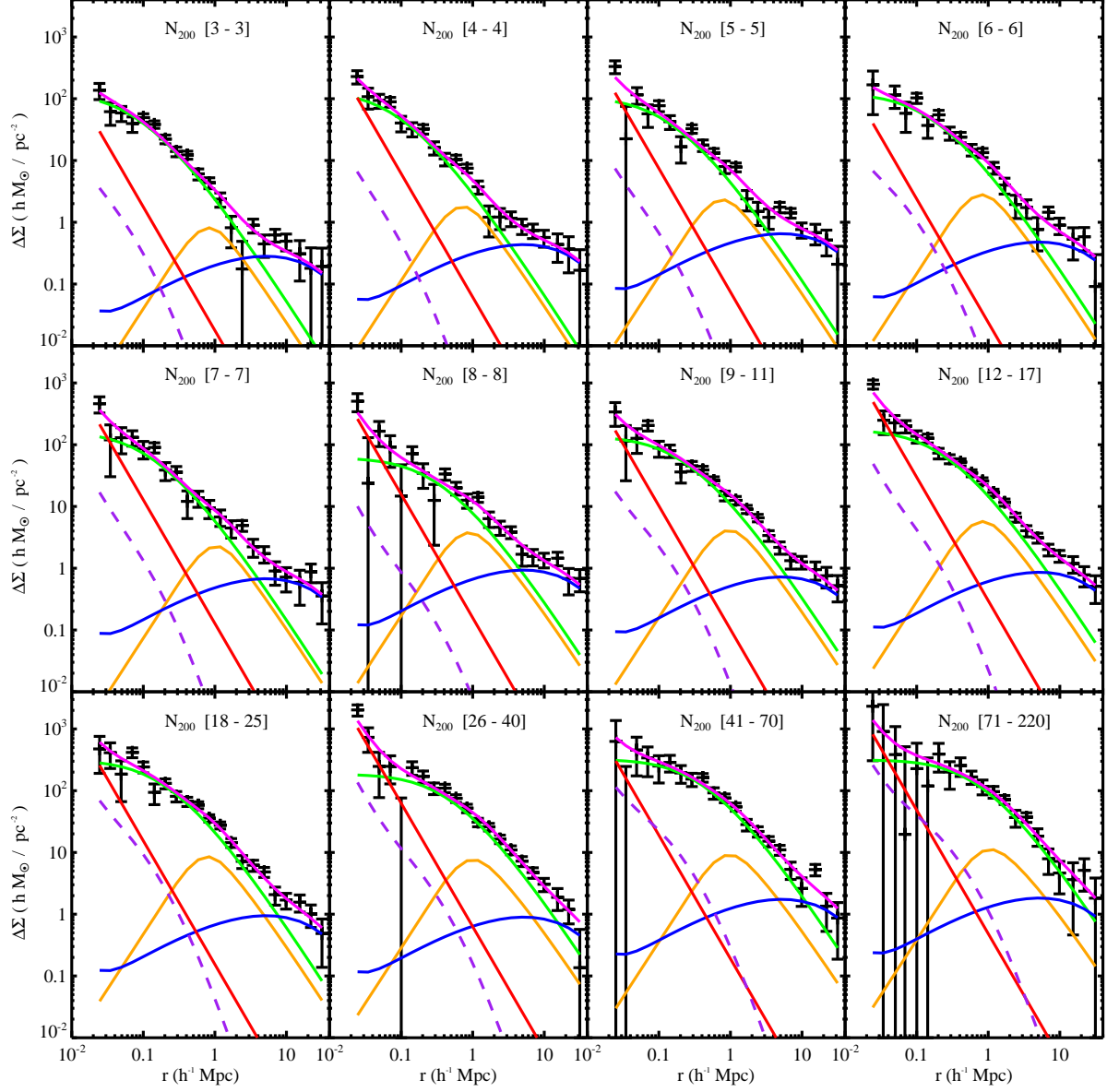
FIG. 8.— Model fits to $\Delta\Sigma(R)$ for the 12 N_{200} richness bins The model components are the NFW halo profile (green), miscentered halo component (orange), the central BCG (red), neighboring halos (blue); the non-linear contribution (purple dashed). The magenta curves show the sum of these components for the best-fit models in each bin.
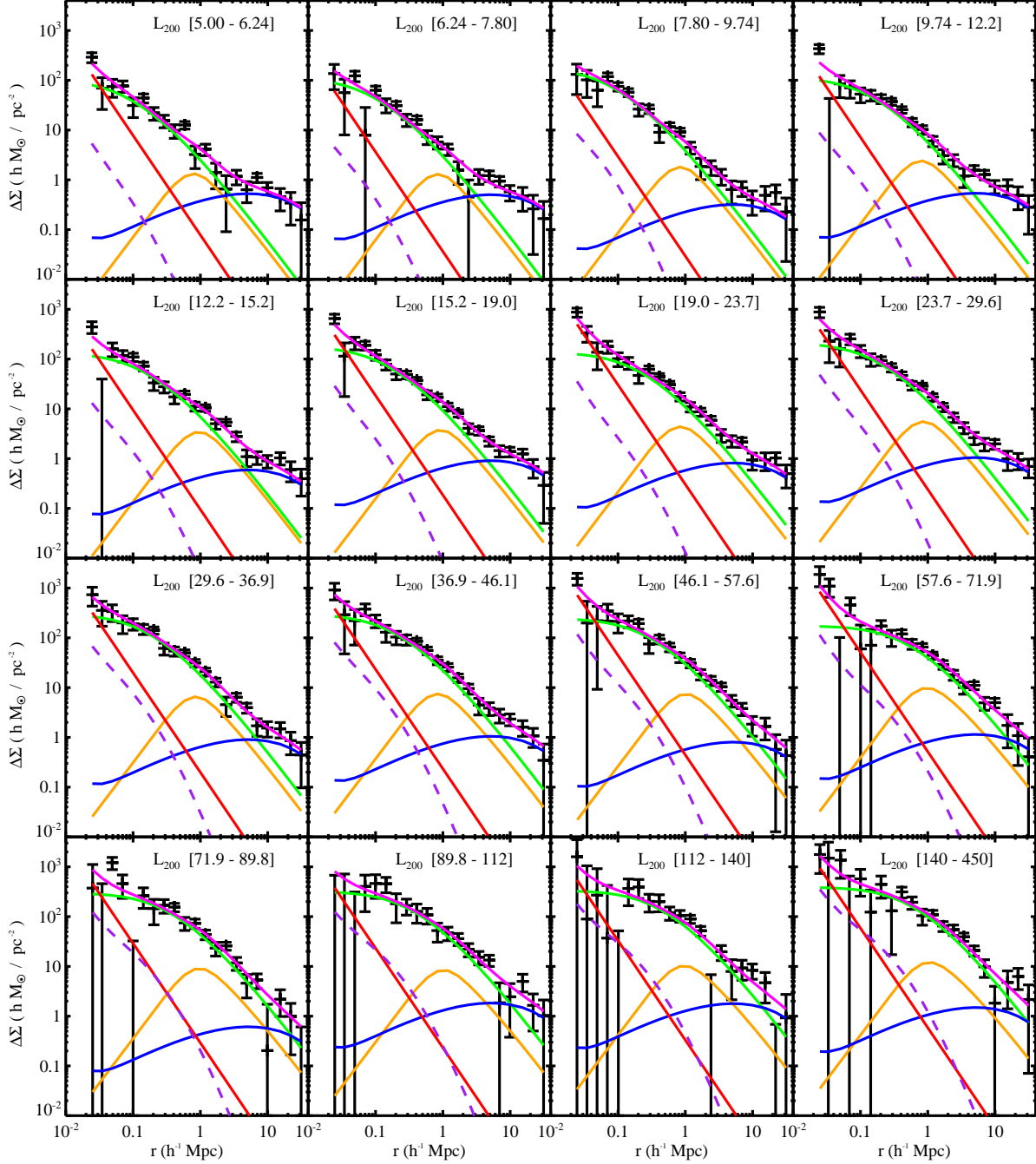
FIG. 9.— Model fits to $\Delta\Sigma(R)$ for the 16 L_{200} luminosity bins. The model components are the NFW halo profile (green), miscentered halo component (orange), the central BCG (red), neighboring halos (blue); the non-linear contribution (purple dashed). The magenta curves show the sum of these components for the best-fit models in each bin.

and shear non-linearity and include only the three parameters c_{200}, M_{200}, and B in the model fits, then the statistical uncertainty in the calibration of the cluster mass–richness relation would be only 3% instead of 5%. However, the halo mass estimates would be biased low by a factor of ~ 1.4. This factor arises because M_{200} is determined mostly by the amplitude of $\Delta\Sigma$ on scales $R \lesssim 1\ h^{-1}$ Mpc, where the smoothed $\Delta\Sigma^s_{NFW}(R)$ makes very little contribution; as a result, ignoring miscentering in fitting to the shear on small scales leads to an under-

estimate of the mass by a factor of $\sim p_c$. From the mock catalogs, we find $\langle p_c \rangle \sim 0.7$, or $1/\langle p_c \rangle \sim 1.4$. Therefore, halo miscentering has a large systematic effect on the estimated halo masses and concentrations and so must be included.

5.2. Halo concentration scaling relations

Figure 12 shows the scaling of the mean concentration c_{200} with halo mass. We have combined the results from both richness (red points) and luminosity bins
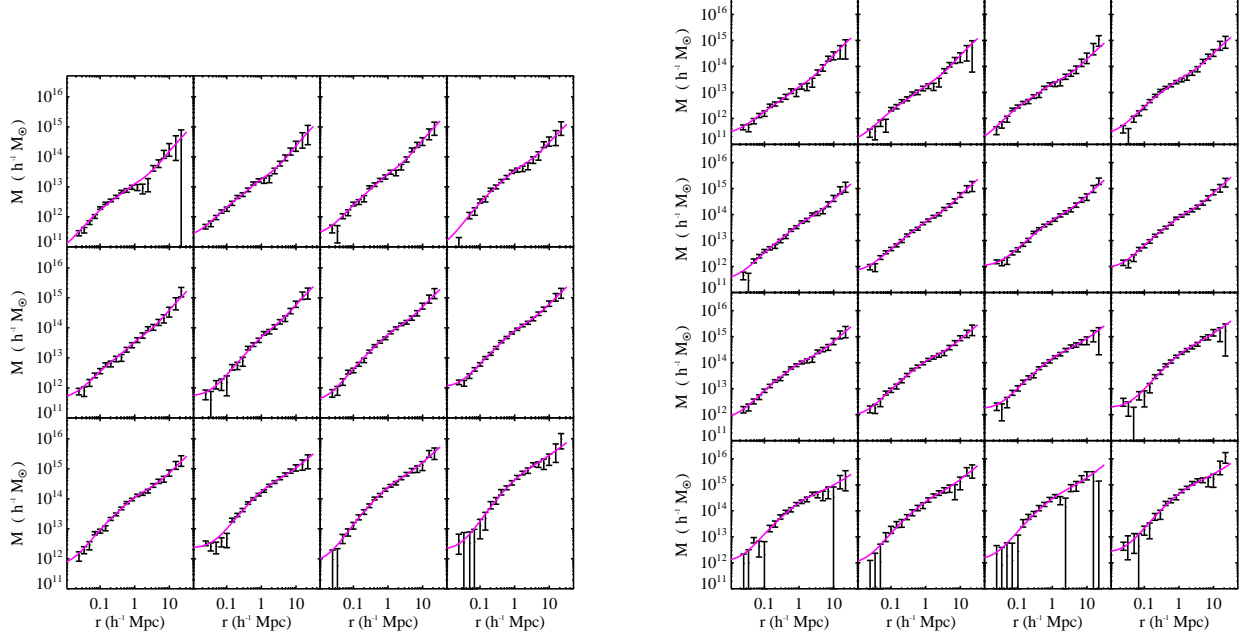
FIG. 10.— The model fits of Fig. 8 and 9 over-plotted on the inverted 3D mass profiles for the 12 N_{200} richness (*left panel*) and 16 L_{200} luminosity bins (*right panel*).
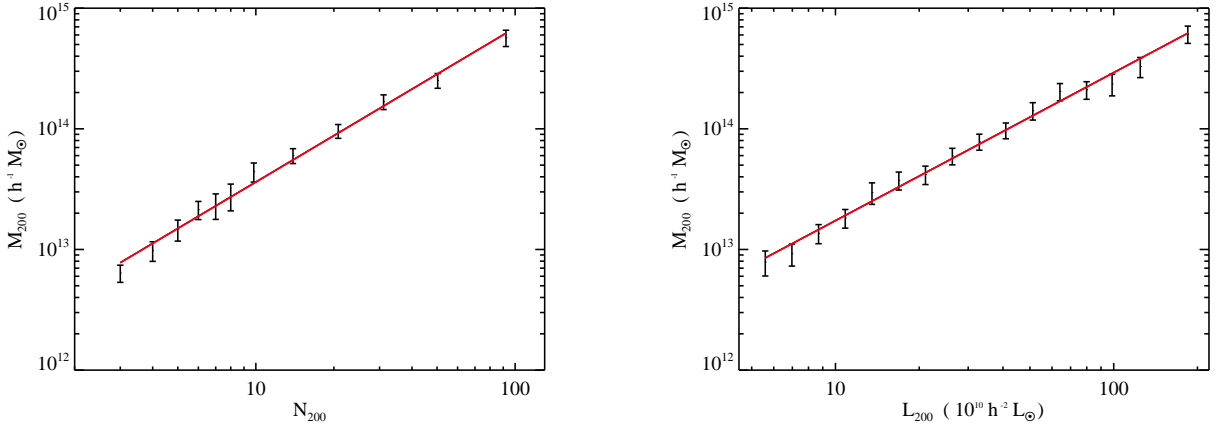

FIG. 11.— The inferred mean halo mass vs. richness (*left panel*) and mass vs. luminosity (it right panel) relations from the model fits to the lensing profiles. The red lines show the best-fit power-law relations (see text).

(black points) on the same plot — these are *not* independent, since the same clusters are used for both. The blue curve shows the best-fit power law,

$$c_{200}(M_{200}) = c_{200|14}(M_{200}/10^{14}h^{-1}M_{\odot})^{\beta_c} \quad (28)$$
$$c_{200|14} = 4.1 \pm 0.2_{stat} \pm 1.2_{sys}$$
$$\beta_c = -0.12 \pm 0.04.$$

The fit is performed with all data points from both binnings but the errors are adjusted upward by $\sqrt{2}$ so that they are not treated as independent data points. These results indicate that the halo concentrations, with typical values $c_{200} \simeq 5$, depend only weakly on halo mass, as has been suggested by previous observational and theoretical results. Note that ignoring the parameters p_c, σ_s and M_0 in the model fits would lead to a (biased) underestimate

of the halo concentration parameter c_{200} by about a factor of 3, as well as to unrealistically small error estimates on the concentration.

For comparison with the lensing results, the green curve in Fig. 12 shows the predicted concentration vs. mass relation from the halo formation model of Bullock et al. (2001). Note that Bullock et al. (2001) use a different definition of halo mass M_{vir} and concentration c_{vir}, so we have converted their predictions to our parameters M_{200} and c_{200} following the translation given in the Appendix. In their model, the halo concentration is given by $c_{vir} = K (a/a_c)$, where $a = 1/(1 + z)$ and a_c is the collapse epoch of the halo; the time at which the typical collapsed mass, M_*, is a fixed fraction F of the halo mass, $M_*(a_c) = F M_{vir}$. This model is defined by the two parameters K and F, which are assumed to be independent

TABLE 10
MASS RICHNESS POWER-LAW FITS: N_{200} BINS

Mass type	$M_{200|20}$	α_N	$c_{200|20}$	β_N
M_{200}	8.794E+13	1.28	3.99	-0.15
M_{180b}	1.204E+14	1.30	6.14	-0.14
M_{vir}	1.055E+14	1.29	5.08	-0.15
M_{500}	6.069E+13	1.25	2.60	-0.16

NOTE. — Coefficients and exponents of the power-law fits of mass and concentration versus richness for the different virial mass definitions. The mass–richness relation and concentration–richness relation is of the form $M = M_{200|20} (N_{200}/20)^{\alpha_N}$ and $c = c_{200|20} (N_{200}/20)^{\beta_N}$. The *relative* errors on parameters are the same as the M_{200} versions (see text).

TABLE 11
MASS RICHNESS POWER-LAW FITS: L_{200} BINS

Mass type	$M_{200|40}$	α_L	$c_{200|40}$	β_L
M_{200}	9.504E+13	1.23	4.37	-0.15
M_{180b}	1.284E+14	1.25	6.68	-0.14
M_{vir}	1.131E+14	1.24	5.54	-0.14
M_{500}	6.672E+13	1.20	2.86	-0.16

NOTE. — Coefficients and exponents of the power-law fits of mass and concentration versus luminosity for the different virial mass definitions. The mass–luminosity relation and concentration–luminosity relation are of the form $M = M_{200|40} (L_{200}/40)^{\alpha_L}$ and $c = c_{200|40} (L_{200}/40)^{\beta_L}$. The *relative* errors on parameters are the same as the M_{200} versions (see text).
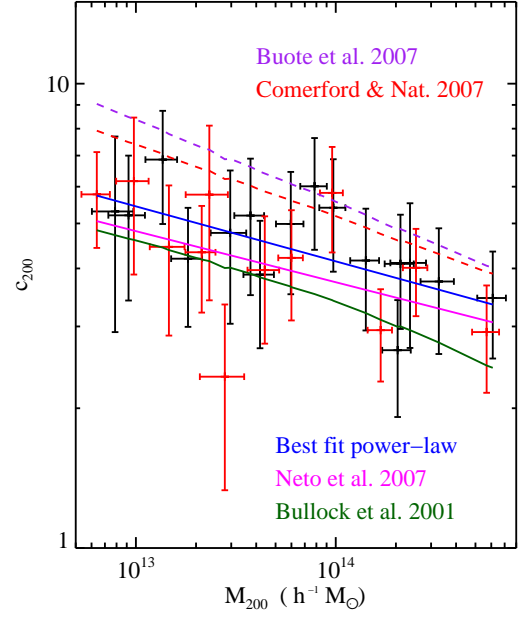

FIG. 12.— The mean NFW halo concentration parameter c_{200} versus halo mass M_{200}. Black points are from the shear profile fits for the L_{200} luminosity bins and the red points are from the N_{200} richness bins. The blue curve shows the best-fit power law to the data (see text). The green curve shows the prediction from the Bullock et al. (2001) model with $F = 0.001$, $K = 2.9$, and our fiducial cosmology. The magenta curve shows the result from Neto et al. (2007) for the Millennium Simulation (adjusted to $z = 0.25$). Note that this was fit to a cosmology with a slightly higher normalization ($\sigma_8 = 0.9$ vs. $\sigma_8 = 0.8$) and is thus expected to have slightly higher concentrations. The purple dashed curve is a result from Buote et al. (2007) on X-ray clusters; the red dashed line shows a result from a compilation of X-ray and strong-lensing clusters (Comerford & Natarajan 2007)

of cosmological parameters. Here M_* is the non-linear mass scale at scale factor a in Press-Schechter theory, i.e., the mass for which $D(a)\sigma(M_*(a)) = \delta_c$, where the linear growth factor $D(a)$ is given by Eqn. 13, δ_c=1.686 is the critical density in the spherical collapse model, and $\sigma(M)$ is the variance of the linear density field smoothed on the scale that on average encloses mass M. We choose the parameter values $K = 2.9$ and $F = 0.001$ (different from the original Bullock numbers), which have been demonstrated to reproduce the measured halo concentrations in a more recent set of LCDM dark matter simulations (Wechsler et al. 2006). With those choices, the predicted concentrations of this galaxy formation model, shown as the green curve in Figure 12, fit those inferred from the lensing data fairly well. The χ^2 between the two is 8 (for 12 degrees of freedom) for the N_{200} richness binning and 12 (for 16 degrees of freedom) for the L_{200} binning. In making this comparison, we have used the fiducial cosmological parameters given at the end of §1. Furthermore, if we keep the Bullock F parameter and cosmological parameters fixed we can determine the best fit Bullock K parameter from our data: $K_{fit} = 3.00 \pm 0.24$ (assuming our fiducial cosmology with $\sigma_8 = 0.8$).

Recently, Neto et al. (2007) studied the concentrations of halos identified from the Millennium Simulation (Springel et al. 2005) and found a power-law relation for the average halo concentration, $c_{200} = 5.26(M_{200}/10^{14}h^{-1}M_\odot)^{-0.1}$. The Millennium simulation uses a flat LCDM cosmology with $\Omega_m = 0.25, \Omega_b = 0.045, h = 0.73, n_s = 1, \sigma_8 = 0.9$ and $z = 0$. Bullock et al. (2001) found that halo concentration scales as $1/(1 + z)$, which is consistent with recent observational results from X-ray clusters ; $c \propto (1 + z)^{-0.71\pm0.52}$ (Schmidt & Allen 2007). We thus shift the Neto et al. (2007) relation by 0.8 to put it at our median cluster redshift of $z = 0.25$; this is shown as the magenta curve in Fig. 12. This result for dissipationless halos agrees very well with both the Bullock et al. (2001) model and our data ($\chi^2 = 8$). Note that because the Neto et al. (2007) results are calculated for a cosmology with slightly higher normalization ($\sigma_8 = 0.9$ vs. $\sigma_8 = 0.8$) they are expected to have slightly higher concentrations and the agreement between the two models is even better than it looks in the figure. The large difference shown in the Neto et al. (2007) paper between their results and the results of Bullock et al. (2001) are due to the fact that these authors used the original Bullock et al. (2001) values for K and F, instead of the updated ones that we use here; with this change the two theoretical models are virtually indistinguishable, and are both in excellent agreement with our results.

Buote et al. (2007) have recently presented a determination of the concentration–mass relation as measured by a set of 39 clusters with X-ray measurements, finding $c_{vir}(1 + z) = (9.0 \pm 0.4)(M vir/M_{14})^{-0.172\pm0.026}$.

This is plotted as the purple-dashed line on Fig. 12. Comerford & Natarajan (2007) also recently compiled several concentration measurements from individual strong-lensing and X-ray clusters (including those of Buote et al. 2007 and Schmidt & Allen 2007), and found $c_{\rm vir}(1 + z) = (14.5 \pm 6.4)(M{\rm vir}/M_*)^{-0.15\pm0.13}$, where $M_* = 1.23\ 10^{12}h^{-1}M_\odot$ at $z = 0.25$ for our fiducial cosmology with $\sigma_8 = 0.8$. This is plotted as the red dashed line on Fig. 12.

In the figure, each of these relations is converted to our M_{200} system for comparison. Both results thus have a mass scaling that is consistent with results; although note that Schmidt & Allen (2007) have seen some indication for a steeping of this power at the highest masses from a sample of X-ray systems.

These results all have a somewhat higher normalization than our data; there are many possibilities for this discrepancy. At least some of the discrepancy is likely due to selection effects between the samples. It is likely that X-ray clusters and strong-lensing clusters are more concentrated than average red-sequence clusters. In the X-ray case, they are chosen to be relaxed systems, which likely have higher concentrations (Wechsler et al. 2002). This effect has been estimated to be of the order ∼ 10–20% (Buote et al. 2007; Schmidt & Allen 2007), but is still somewhat uncertain. Very concentrated clusters will be also more likely to produce strong-lensing features. Also, the X-ray flux is proportional to the square of the gas density and so X-ray selection also favors more concentrated clusters. It is also possible that our model for miscentering is underestimated, which would reduce our modeled concentrations compared to the true halo concentrations. We may be able to better constrain the miscentering the future, and are also working towards measurements with a clearly well-centered cluster sample to further investigate these effects.

Mandelbaum et al. (2006) constrains the concentration of typical halos containing SDSS luminous red galaxies with galaxy-galaxy lensing. They find $c_{180b} = 5.6\pm0.6$ which is $c_{200} = 3.8 \pm 0.4$, consistent with our results.

5.3. *Bias scaling relations*

Figure 13 shows the scaling of the mean effective bias parameter B as a function of halo mass. The lensing results are well fit by a power law, indicated by the blue solid curve,

$$B(M_{200}) = B_{200|14}\ (M_{200}/10^{14}h^{-1}M_\odot)^{\alpha_B} \quad (29)$$
$$B_{200|14} = (0.26 \pm 0.02_{stat} \pm 0.02_{sys})$$
$$\alpha_B = 0.38 \pm 0.02$$

The fit is performed with all data points from both binnings but the errors are adjusted upward by $\sqrt{2}$ so that they are not treated as independent data points. As theoretically expected, the clustering strength, i.e., the bias, increases with halo mass.

As above, it is of interest to compare these results with the predictions of structure formation models. The halo bias can be computed using the "peak-background split" (Mo et al. 1996; Sheth & Tormen 1999). We consider the model of Sheth et al. (2001), which is derived from the elliptical collapse model and calibrated with N-body simulations. In their bias relation, the halo mass is defined in terms of the region within which the mean density
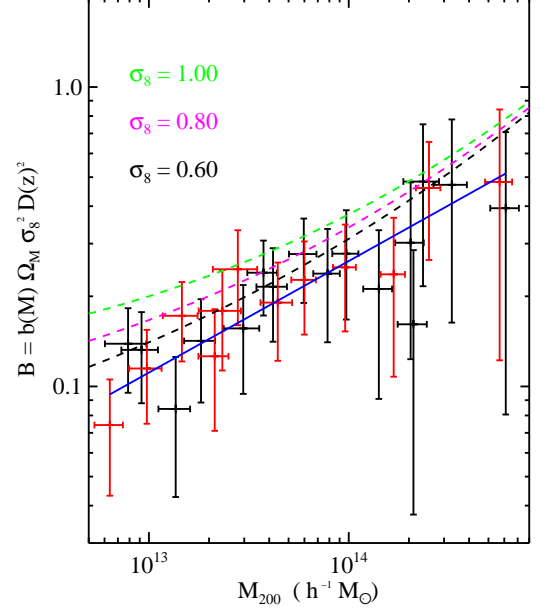

FIG. 13.— The effective bias parameter (the coefficient of the two-halo term) $B = b(M_{200})\Omega_m\sigma_8^2 D^2(z)$ versus M_{200}: black points show lensing results in luminosity bins, red in N_{200} bins. The blue curve is the best-fit power law (see text). The three dotted curves show the predictions from the Sheth et al. (2001) elliptical collapse model for three values of σ_8: (1.0, 0.8, 0.6), from top to bottom.

is 180 times the mean density of the Universe at redshift z, $M_{180b} = M(r_{180b}) = 4/3\pi r_{180b}^3 180\bar{\rho}(z)$. Using the formulas of the Appendix, we convert between this definition and our expression for M_{200} given in Eqn. 4. The Sheth et al. (2001) halo bias relation is given by

$$b(\nu) = 1 + \frac{1}{\sqrt{a}\delta_c} \times$$
$$\left[\sqrt{a}(a\nu^2) + b\sqrt{a}(a\nu^2)^{1-c} - \frac{(a\nu^2)^c}{(a\nu^2)^c + b(1-c)(1-c/2)}\right] \quad (30)$$

where $\delta_c = 1.686$ and $\nu = \delta_c/(D(z)\sigma(M))$. Sheth et al. (2001) chose parameters $a = 0.707, b = 0.5$, and $c = 0.6$ to agree with N-body simulations. However, both Seljak & Warren (2004b) and Tinker et al. (2005) determined that this relation over-estimates the bias at fixed halo mass by about 20%, especially for masses less than the non-linear mass scale M_*. Tinker et al. (2005) find that this expression gives a better fit to the simulations for $a = 0.707, b = 0.35$, and $c = 0.8$, and we adopt these parameter values to compare with the lensing results.

One effect that needs to be included is that we are not measuring $B(M_{200})$ exactly but rather $\langle B(M_{200})\rangle$ where the average is over the log-normal distribution of mass. Similarly, we are plotting these versus $\langle M_{200}\rangle$. Therefore, to compare the theoretical predictions to the data we need to multiply the theoretical predictions at $\langle M_{200}\rangle$ by $\langle B\rangle / B(\langle M_{200}\rangle)$ which is $\exp(V_M\ \alpha_B(\alpha_B - 1)/2)$ for a log-normal distribution. Here, $\alpha_B = 0.38$, is the logarithmic slope $B(M_{200}) \sim M_{200}^{\alpha_B}$ and V_M is the variance of $\ln M_{200}$. This correction varies with richness but is typically about 10% and adds about $5 - 10\%$ uncertainty to the predictions depending on the width of the prior dis-

tribution for V_M. With our (probably overly generous) prior of 0.6 for $\ln V_M$, this uncertainty is 10%.

The resulting theoretical expressions for B are plotted as the dashed lines (black, magenta, and green) in Fig. 13 for three values of σ_8: $0.6, 0.8,$ and 1.0. These correspond to non-linear masses, M_*: $0.43, 1.23,$ and $5.26 \times 10^{12} h^{-1} M_\odot$ at $z = 0.25$. Although the predictions for all three choices are within $\sim 30\%$ of the best-fit relation from lensing, the data appear to prefer lower values of σ_8. The χ^2s are acceptable for both $\sigma_8 = 0.6$ ($\chi^2_N = 7, \chi^2_L = 12$) and $\sigma_8 = 0.8$ ($\chi^2_N = 15, \chi^2_L = 20$) but formally unacceptable for $\sigma_8 = 1$ ($\chi^2_N = 32, \chi^2_L = 36$). The number of degrees of freedom is 12 and 16 for χ^2_N and χ^2_L respectively. These χ^2 numbers do *not* include the above mentioned V_M uncertainty and so can be reduced by another 10-20%. We refrain from drawing cosmological conclusions from this comparison for several reasons. First, in fitting the halo model to the lensing results, we assumed particular values for the cosmological parameters (except σ_8) when we calculated the linear correlation function ξ_l (Eqn. 14) for the two-halo term. For a self-consistent cosmological constraint, we would need to float the cosmological parameters in calculating the two-halo term for the lens model fit. It would also be desirable to allow for possible scale-dependent bias, since the predicted non-linear correlation function at the largest scales we probe, $25 - 40\ h^{-1}$ Mpc, differs slightly from the linear theory prediction (Smith et al. 2007). We would also want to consider halo-exclusion effects (Zheng 2004). We believe that precise prediction of the bias involving all of these effects at these intermediate scales is not yet possible but clearly the quality of data is improving to the point where such study is now warranted.

It would be better to extend the lensing measurements to slightly larger scales ($\geq 50\ h^{-1}$ Mpc comoving) in order to reduce this effect and, more importantly, to isolate the large-scale bias measurements from degeneracies with the NFW halo parameters. Finally, to reliably estimate cosmological parameters we would require data with better signal-to-noise ratios as well as more precise shear and photometric redshift calibration. In future wide-area, deeper lensing surveys, these conditions will all be met, and constraints on cosmology from lensing measurements of the halo bias will be possible.

5.4. *BCG–halo mass scaling relation*

We have included this point mass term in our model mostly to allow enough freedom so that the concentration measurements would not be overly influenced by the first few data points. This is especially important when non-linear shear is considered. However, the relation between the BCG mass and the central halo mass may be of interest in itself. Figure 14 shows the point mass term, M_0, plotted versus the mean central halo mass, M_{200}. The point mass increases with central halo mass but seems to plateau at an asymptotic mass of about $1.3 \times 10^{12} h^{-1} M_\odot$. The blue curve is simply a fitting function: $M_0 = p_0/(1 + (M_{200}/p_1)^{p_2})$ with best fit values $p_0 = 1.334 \times 10^{12} h^{-1} M_\odot$, $p_1 = 6.717 \times 10^{13} h^{-1} M_\odot$ and $p_2 = -1.380$. These masses are consistent with the expected masses of galaxy halos. Strong-lensing constrains (e.g. Rusin et al. (2003)) show that nearly every strong lens is well fit by an singular isothermal
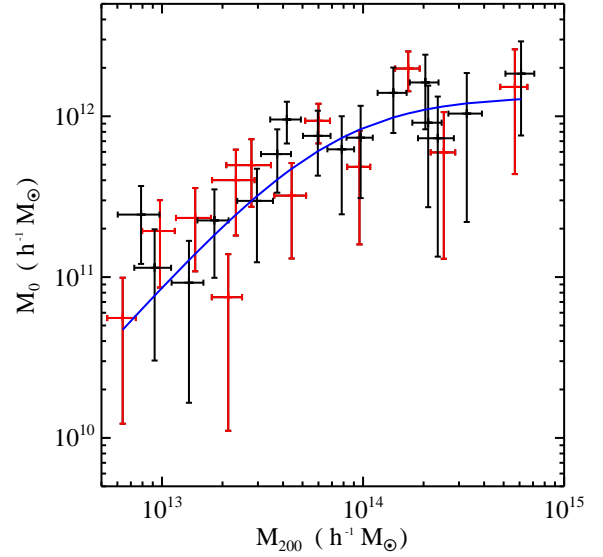

FIG. 14.— The BCG point mass vs. mean central halo mass for both richness bins: N_{200} (red) L_{200} (black). The point mass term increases with central halo mass at low halo mass but flattens out at about $10^{12} h^{-1} M_\odot$. The blue curve is a fitting function: $M_0 = p_0/(1 + (M_{200}/p_1)^{p_2})$ with $p_0 = 1.334\ 10^{12} h^{-1} M_\odot$, $p_1 = 6.717\ 10^{13} h^{-1} M_\odot$ and $p_2 = -1.380$. The point mass is roughly consistent with the masses of luminous red galaxies from strong-lensing constraints.

sphere out to at least $100 h^{-1}$ kpc. The 3D mass of a singular isothermal sphere is given by $M_{SIS}(r) = 4.64 \times 10^{12}\ h^{-1} M_\odot\ (\sigma_s/100\ \text{km/s})^2\ (r/\text{Mpc})$ which at $25 h^{-1}$ kpc gives $1.2 \times 10^{11}, 4.6 \times 10^{11}$ and $1 \times 10^{12} h^{-1} M_\odot$ for stellar velocity dispersions, $\sigma_s = 100, 200$ and 300 km/s respectively. This mass range agrees well with our point-mass values. This comparison is inexact since SISs and point masses have different shear profiles. A precise measurement of the mass density of the central BCG would be better suited to a combination of strong and weak lensing (e.g. Gavazzi et al. (2007)) and is beyond the scope of this paper.

6. COMPARISON OF LENSING AND DYNAMICAL MASS MEASUREMENTS

Becker et al. (2007) have recently estimated statistical masses of MaxBCG clusters from the Koester et al. (2007b) catalog from stacked velocity dispersion measurements. Using galaxies near each BCG with measured spectroscopic redshifts, they build a richness-dependent histograms of velocity differences and fit the shape to a summed, log-normally distributed, set of Gaussians. Results show that the geometric mean velocity dispersion scales as a power law, $\sigma_v \sim N_{200}^{0.436 \pm 0.015}$, with a log-normal dispersion that declines from 0.40 ± 0.02 at $N_{200} = 10$ to 0.15 ± 9 at $N_{200} = 88$. Although the typical maxBCG cluster contains few galaxies with spectroscopic redshifts, it is the case that, as with cross-correlation lensing, the velocity histograms can be stacked from many clusters within a richness bin to build a high signal-to-noise histogram of the average velocity differences. The best-fit velocity dispersion implies a mass, M_{200}, derived from the dark matter virial relation, $\sigma_{DM}(M_{200}, z) = (1082.9 \pm 4.0\ \text{km/s})(h(z)M_{200}/10^{15} M_\odot)^{0.3361 \pm 0.0026}$, calibrated re-
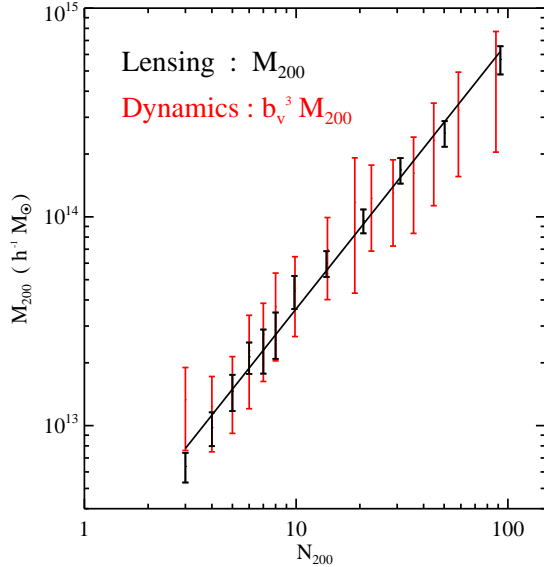
FIG. 15.— Mean halo mass vs. richness from the lensing profiles (black points, the same as those shown in Fig. 11) and from dynamical galaxy velocity dispersion measurements (red points) from the same cluster sample (Becker et al. 2007). The two scaling relations are in good agreement, although the lensing data provides a tighter relation. Black curve shows the best-fit power-law relation from the lensing data.

cently from a suite of N-body simulations (Evrard et al. 2007). Galaxy and dark matter dynamics may differ, and this potentiality is approximately treated as a constant velocity bias parameter, $b_v \equiv \sigma_v/\sigma_{\rm DM}$. Figure 15 shows the mean virial mass estimates from the dynamical measurements in red and the lensing halo masses (from Fig. 11) in black. The line shows the best-fit, power-law relation from the lensing masses. The Becker et al. (2007) error bars include systematic errors inherent in their method, and are correlated. The statistical lensing and dynamical mass estimates appear in very good agreement, but systematic uncertainties in b_v remain to be understood. When Becker et al. (2007) tested their virial mass estimator on mock SDSS maxBCG catalogs, they found it to systematically underestimate halo masses by 25%. This correction factor has not been applied to the estimates in Fig. 15. Including it would elevate $b_v^3 M_{\rm vir}$ above the lensing masses, suggesting a positive velocity bias, $b_v \simeq 1.1$. The current level of agreement indicates that the velocity bias parameter is not significantly different from unity. We defer a more formal analysis of these issues to future work.

7. DISCUSSION

In Paper I of this series, we demonstrated that cross-correlation weak lensing can be measured around clusters of galaxies out to large radii, $R \sim 30\ h^{-1}$ Mpc. In this work, we have shown that these mean shear profiles are well described by realistic models derived from N-body simulations. Our primary results are the lensing calibration of the cluster halo mass–richness and mass–luminosity relations and measurements of the scaling relations between the mass, bias, and concentration of halos. We also show that lensing-inferred masses are consistent with estimates from stacked velocity dispersion measurements (Becker et al. 2007) as long as the velocity bias

parameter is not significantly different from unity. The scaling relation between halo concentration and mass that we derive from lensing agrees well with the results of N-body simulations (e.g., the model of Bullock et al. 2001 as updated by Wechsler et al. 2006, or the recent results of Neto et al. 2007). The scaling between halo bias and mass from lensing is in agreement with the simulation-calibrated predictions of (Sheth et al. 2001).

In this work, we have limited the analysis to the modeling of the lensing profiles. However, for completeness we now describe some cosmological applications of these results that are now possible. We then conclude by suggesting some applications of these methods that will be possible with the ambitious wide-field surveys now being planned.

Perhaps the most obvious application of the measured halo mass–richness relation is to measurement of the mass function of clusters. Previously, Rozo et al. (2007b) completed a first analysis constraining cosmology through the cluster mass function using the same SDSS cluster catalog. They modeled the mass–richness relation using the Halo Occupation Distribution (HOD) model, without a strong observational prior on the mass–richness relation itself. In this model, one adopts a parametrized mass–richness relation, and Rozo et al. (2007b) employed tight cosmic microwave background and SN Ia priors on cosmological parameters *except* for σ_8, for which only a non-informative prior was used. They found $\sigma_8 = 0.92 \pm 0.1$ and derived constraints on the HOD model parameters. This method (Rozo et al. 2007a) employs marginalization over a generous supply of nuisance parameters that connect the observables to mock catalog predictions (Wechsler et al. in preparation). While Rozo et al. (2007b) represents one of the more robust measurements of σ_8 from the cluster mass function, an update to this work using the mass–richness relation derived from lensing is in progress. This should allow for tighter constraints on σ_8, a tight constraint on Ω_m, as well as a more precise measurement of the HOD parameters.

Mandelbaum & Seljak (2007) have put a lower bound on $\sigma_8(\Omega_m/0.25)^{0.5} > 0.62$ at 95% C.L. by employing a method simpler than full modeling of cluster number counts. They argue that the lensing signal around a sample of isolated luminous red galaxies in the SDSS could not be produced by low values of σ_8 since too few clusters would have formed. Interpretational complications such as incompleteness of the cluster sample or miscentering would only decrease the predicted signal, so their bound should be robust.

There are several ways in which measurements of stacked lensing profiles around clusters can be used to derive entirely new constraints on cosmology. The amplitude of the linear galaxy or cluster auto-correlation function measures the combination $b^2\sigma_8^2 D^2(z)$, whereas lensing measures $b\sigma_8^2 D^2(z)\Omega_m$. Combining both galaxy or cluster auto-correlations with lensing will thus allow one to measure the two combinations $\Omega_m\sigma_8 D(z)$ and b/Ω_m. By combining these two measurements into an estimate of $\Omega_m\sigma_8 D(z)$, it is possible to directly probe the growth of structure. The linear growth factor is sensitive to cosmological parameters affecting the Hubble parameter, such as Ω_m, as well as to dark energy and spatial curvature. This growth measurement would com-

plement geometric probes of dark energy such as type Ia supernovae and baryon acoustic oscillations. In addition, this measurement of the growth factor would complement cluster number counts since it extracts information from much larger scales. Measuring dark energy through this direct measurement of the growth factor would have very different systematics from both cosmic shear and cluster number counts. This measurement will most likely require lensing measurements extending to slightly larger scales, $50-100h^{-1}$ Mpc, to better tie down the B parameter, as well as more attention to systematic errors such as shear calibration and photo-z biases. Since it relies on large-scale information, it will require a deep survey over a large fraction of the sky to reduce the cosmic variance to a small enough level to compete with the other methods.

Seljak et al. (2005) employed a similar technique to constrain σ_8 by using lensing to constrain halo masses so that halo biases could be predicted and used to "de-bias" the galaxy power spectrum. This however requires the complication of HOD modeling to connect galaxies to the halos that they occupy. It could be simpler to apply this idea directly to clusters, since this requires only large-scale auto-correlation function (or power spectrum) measurements and does not require large-scale lensing measurements. This approach does, however, rely on models for the bias prediction (e.g. Sheth & Tormen 1999; Seljak & Warren 2004b), so direct measurement of the bias would be preferred as long as the errors are sufficiently small.

Future weak lensing surveys such as SNAP (SNAP Collaboration 2005), DUNE (Réfrégier et al. 2006), LSST (Tyson et al. 2002) and DES (Dark Energy Survey Collaboration 2005). would be ideal for these types of measurements. The statistical errors on the average shear in a radial bin should be at the percent level for these surveys, compared to 50% for the SDSS cluster data for identical binning. Since the dark energy constraints from measurement of the shear power spectrum will already require shear calibration and photo-z biases below the percent level, this would suggest that these surveys should be able to measure halo masses, concentrations, and biases at about the percent level for perhaps hundreds of richness bins. Entirely new ways of using lensing to constrain cosmology may be possible. For example, baryon acoustic oscillations should leave their imprint on the $\Delta\Sigma$ profile at comoving scales of $100h^{-1}$ Mpc and will be detectable with surveys such as these. Determining how to extract the most information from such a data set should remain a fruitful area of study.

APPENDIX

"Virial-type" mass definitions all have the form

$$M_a = M(r_a) = \frac{4\pi}{3} r_a^3 \ \Delta_a \ \rho_a \ , \tag{1}$$

where $M(r)$ is the mass profile. The number Δ_a may be a function of cosmology and redshift. Typical choices for Δ_a are 200 and 180. The density ρ_a is always some variation of the critical density, ρ_{crit}, but it may be $\rho_{crit}(z)$ or $\bar{\rho}(z) = \rho_{crit}(z=0) \ (1+z)^3$. Let us define $D_a \equiv \Delta_a \ \rho_a$, since the conversion between different conventions only depends on this product.

For any two choices of D_a, there is a conversion between them for the mass M_a, (or equivalently r_a) and the NFW concentration parameter c_a. M_a and c_a (unlike r_s and r_a) are independent of the choice between *physical* and *comoving* units.

Hu & Kravtsov (2003) discuss this issue but we will review the conversion again here.

The NFW form for the density profile is given by

$$\rho(r) = \frac{\rho_s}{(r/r_s) \ (1 + r/r_s)^2} \ . \tag{2}$$

Under this assumption, the mass profile for some choice of mass definition is given by

$$M(r) = 4\pi \rho_s r_a^3 \ f(r_s/r_a) \ , \tag{3}$$

where

$$f(x) = x^3 \left[\ln(1 + x^{-1}) - (1 + x)^{-1} \right] \ , \tag{4}$$

and the concentration is defined as $c_a = r_a/r_s$. The parameters r_s and ρ_s are independent of the choice of D_a, so for any other choice D_b we have $3\rho_s = D_a/f(1/c_a) = D_b/f(1/c_b)$. Therefore we have the conversion between the two concentrations,

$$1/c_b = f^{-1}\left(\frac{D_b}{D_a}\ f(1/c_a)\right)\ . \tag{5}$$

Similarly, $r_s = r_a/c_a = r_b/c_b$, so the conversion for these "virial" radii is $r_b = r_a c_b/c_a$, and the conversion between masses is

$$M_b = M_a\ \frac{D_b}{D_a}\ \left(\frac{c_b}{c_a}\right)^3\ . \tag{6}$$

The inverse function of f needs to be computed with a look-up table and interpolation since a simple closed-form expression does not exist. However, the conversion simply depends on the ratio D_b/D_a.

An as example, we consider the two most common choices, $D_{200c} = 200\rho_{crit}(z) = 200\rho_{crit}(0)H^2(z)/H_0^2 = 200\rho_{crit}(0)[\Omega_m(1+z)^3 + (1-\Omega_m)]$ (in a flat LCDM universe) and $D_{180b} = 180\bar{\rho}(z) = 180\rho_{crit}(0)(1+z)^3\ \Omega_m$. The ratio of these is

$$\frac{D_{180b}}{D_{200c}} = \frac{9}{10}\ \Omega_m(z) = \frac{9}{10}\ \frac{\Omega_m\ (1+z)^3}{\Omega_m\ (1+z)^3 + (1-\Omega_m)} \tag{7}$$

We use this formula to convert our measured masses M_{200c} to M_{180b}, using $z = 0.25$ and $\Omega_m = 0.27$, which gives $D_{180b}/D_{200c} = 0.377$. We use this conversion to compute the halo bias, since it has been shown to be nearly universal when expressed in the D_{180b} mass definition.

Similarly, to calculate the halo concentration using the Bullock et al. (2001) model, we need to convert M_{200} to M_{vir}. This conversion uses (Bryan & Norman 1998)

$$\Delta_{vir} \equiv \frac{18\pi^2 + 82x - 39x^2}{1+x}\ , \tag{8}$$

with $x \equiv \Omega_m(z) - 1$. This results in

$$\frac{D_{vir}}{D_{200c}} \equiv \frac{18\pi^2 + 82x - 39x^2}{200}\ . \tag{9}$$

REFERENCES

Allen, S. W., Rapetti, D. A., Schmidt, R. W., Ebeling, H., Morris, G., & Fabian, A. C. 2007, ArXiv e-prints, 0706.0033 [astro-ph]

Bahcall, N. A. et al. 2003, ApJ, 585, 182

Becker, M. R., McKay, T. A., Koester, B., Wechsler, R. H., Rozo, E., Evrard, A., Johnston, D., Sheldon, E., Annis, J., Lau, E., Nichol, R., & Miller, C. 2007, ArXiv e-prints, 0704.3614 [astro-ph]

Blanton, M. R., et al. 2003, ApJ, 592, 819

Bradač, M., Clowe, D., Gonzalez, A. H., Marshall, P., Forman, W., Jones, C., Markevitch, M., Randall, S., Schrabback, T., & Zaritsky, D. 2006, ApJ, 652, 937

Bradač, M., Lombardi, M., & Schneider, P. 2004, A&A, 424, 13

Brainerd, T. G., Blandford, R. D., & Smail, I. 1996, ApJ, 466, 623

Bryan, G. L. & Norman, M. L. 1998, ApJ, 495, 80

Bullock, J. S., Kolatt, T. S., Sigad, Y., Somerville, R. S., Kravtsov, A. V., Klypin, A. A., Primack, J. R., & Dekel, A. 2001, MNRAS, 321, 559

Buote, D. A., Gastaldello, F., Humphrey, P. J., Zappacosta, L., Bullock, J. S., Brighenti, F., & Mathews, W. G. 2007, ApJ, 664, 123

Carlstrom, J. E., Holder, G. P., & Reese, E. D. 2002, ARA&A, 40, 643

Clowe, D., Bradač, M., Gonzalez, A. H., Markevitch, M., Randall, S. W., Jones, C., & Zaritsky, D. 2006, ApJ, 648, L109

Clowe, D., Luppino, G. A., Kaiser, N., Henry, J. P., & Gioia, I. M. 1998, ApJ, 497, L61

Cohn, J. D., Evrard, A. E., White, M., Croton, D., & Ellingson, E. 2007, ArXiv e-prints, 0706.0211 [astro-ph]

Comerford, J. M. & Natarajan, P. 2007, MNRAS, 379, 190

Cypriano, E. S., Sodré, L. J., Kneib, J., & Campusano, L. E. 2004, ApJ, 613, 95

Dark Energy Survey Collaboration. 2005, arXiv:astro-ph/0510346

de Putter, R. & White, M. 2005, New Astronomy, 10, 676

Diemand, J., Moore, B., & Stadel, J. 2004, MNRAS, 352, 535

Eisenstein, D. J. & Hu, W. 1998, ApJ, 496, 605

Eisenstein, D. J. et al. 2005, ApJ, 633, 560

Eke, V. R., Navarro, J. F., & Steinmetz, M. 2001, ApJ, 554, 114

Evrard, A. E., Bialek, J., Busha, M., White, M., Habib, S., Heitmann, K., Warren, M., Rasia, E., Tormen, G., Moscardini, L., Power, C., Jenkins, A. R., Gao, L., Frenk, C. S., Springel, V., White, S. D. M., & Diemand, J. 2007, arXiv:astro-ph/0702241

Evrard, A. E., MacFarland, T. J., Couchman, H. M. P., Colberg, J. M., Yoshida, N., White, S. D. M., Jenkins, A., Frenk, C. S., Pearce, F. R., Peacock, J. A., & Thomas, P. A. 2002, ApJ, 573, 7

Evrard, A. E., Metzler, C. A., & Navarro, J. F. 1996, ApJ, 469, 494

Fahlman, G., Kaiser, N., Squires, G., & Woods, D. 1994, ApJ, 437, 56

Fischer, P., McKay, T. A., Sheldon, E., et al. 2000, AJ, 120, 1198

Gavazzi, R., Treu, T., Rhodes, J. D., Koopmans, L. V. E., Bolton, A. S., Burles, S., Massey, R., & Moustakas, L. A. 2007, arXiv:astro-ph/0701589

Grego, L. et al. 2001, ApJ, 552, 2

Gunn, J. E. & Gott, J. R. I. 1972, ApJ, 176, 1

Haiman, Z., Mohr, J. J., & Holder, G. P. 2001, ApJ, 553, 545

Hallman, E. J., Motl, P. M., Burns, J. O., & Norman, M. L. 2006, ApJ, 648, 852

Hammer, F. 1991, ApJ, 383, 66

Hansen, S. M., McKay, T. A., Wechsler, R. H., Annis, J., Sheldon, E. S., & Kimball, A. 2005, ApJ, 633, 122

Hoekstra, H. 2003, MNRAS, 339, 1155

Hu, W. & Kravtsov, A. V. 2003, ApJ, 584, 702

Huterer, D. & Turner, M. S. 2001, Phys. Rev. D, 64, 123527

Irgens, R. J., Lilje, P. B., Dahle, H., & Maddox, S. J. 2002, ApJ, 579, 227

Joffre, M. et al. 2000, ApJ, 534, L131

Johnston, D. E., Sheldon, E. S., Tasitsiomi, A., Frieman, J. A., Wechsler, R. H., & McKay, T. A. 2007, ApJ, 656, 27

Kaiser, N. 1984, ApJ, 284, L9

Kneib, J.-P., Ellis, R. S., Smail, I., Couch, W. J., & Sharples, R. M. 1996, ApJ, 471, 643

Koester, B. P., McKay, T. A., Annis, J., Wechsler, R. H., Evrard, A. E., Rozo, E., Bleem, L., Sheldon, E. S., & Johnston, D. 2007a, ApJ, 660, 221

Koester, B. P. et al. 2007b, ApJ, 660, 239

LaRoque, S. J., Bonamente, M., Carlstrom, J. E., Joy, M. K., Nagai, D., Reese, E. D., & Dawson, K. S. 2006, ApJ, 652, 917

Levine, E. S., Schulz, A. E., & White, M. 2002, ApJ, 577, 569

Lilly, S. J., Le Fevre, O., Crampton, D., Hammer, F., & Tresse, L. 1995, ApJ, 455, 50

Luppino, G. A. & Kaiser, N. 1997, ApJ, 475, 20

Macciò, A. V., Dutton, A. A., van den Bosch, F. C., Moore, B., Potter, D., & Stadel, J. 2007, MNRAS, 378, 55

Mandelbaum, R. & Seljak, U. 2007, Journal of Cosmology and Astro-Particle Physics, 6, 24

Mandelbaum, R., Seljak, U., Cool, R. J., Blanton, M., Hirata, C. M., & Brinkmann, J. 2006, MNRAS, 372, 758

Mandelbaum, R., Tasitsiomi, A., Seljak, U., Kravtsov, A. V., & Wechsler, R. H. 2005, MNRAS, 362, 1451

Markevitch, M. & Vikhlinin, A. 2007, Phys. Rep., 443, 1

Massey, R., Heymans, C., Bergé, J., Bernstein, G., Bridle, S., Clowe, D., Dahle, H., Ellis, R., Erben, T., Hetterscheidt, M., High, F. W., Hirata, C., Hoekstra, H., Hudelot, P., Jarvis, M., Johnston, D., Kuijken, K., Margoniner, V., Mandelbaum, R., Mellier, Y., Nakajima, R., Paulin-Henriksson, S., Peeples, M., Roat, C., Refregier, A., Rhodes, J., Schrabback, T., Schirmer, M., Seljak, U., Semboloni, E., & van Waerbeke, L. 2007, MNRAS, 376, 13

Metzler, C. A., White, M., & Loken, C. 2001, ApJ, 547, 560

Metzler, C. A., White, M., Norman, M., & Loken, C. 1999, ApJ, 520, L9

Mo, H. J., Jing, Y. P., & White, S. D. M. 1996, MNRAS, 282, 1096

Motl, P. M., Hallman, E. J., Burns, J. O., & Norman, M. L. 2005, ApJ, 623, L63

Nagai, D. 2006, ApJ, 650, 538

Nagai, D. & Kravtsov, A. V. 2005, ApJ, 618, 557

Nagai, D., Vikhlinin, A., & Kravtsov, A. V. 2007, ApJ, 655, 98

Navarro, J. F., Frenk, C. S., & White, S. D. M. 1997, ApJ, 490, 493

Neto, A. F., Gao, L., Bett, P., Cole, S., Navarro, J. F., Frenk, C. S., White, S. D. M., Springel, V., & Jenkins, A. 2007, arXiv:, 0706.2919 [astro-ph]

Newman, J. A., Marinoni, C., Coil, A. L., & Davis, M. 2002, PASP, 114, 29

Press, W. H. & Schechter, P. 1974, ApJ, 187, 425

Réfrégier, A. et al. 2006, in Presented at the Society of Photo-Optical Instrumentation Engineers (SPIE) Conference, Vol. 6265, Space Telescopes and Instrumentation I: Optical, Infrared, and Millimeter. Edited by Mather, J ohn C.; MacEwen, Howard A.; de Graauw, Mattheus W. M.. Proceedings of the SPIE, Volume 6265, pp. 62651Y (20 06).

Reiprich, T. H. & Böhringer, H. 2002, ApJ, 567, 716

Rozo, E., Wechsler, R. H., Koester, B. P., Evrard, A. E., & McKay, T. A. 2007a, ApJ, submitted, arXiv:astro-ph/0703574

Rozo, E., Wechsler, R. H., Koester, B. P., McKay, T. A., Evrard, A. E., Johnston, D., Sheldon, E. S., Annis, J., & Frieman, J. A. 2007b, ApJ, submitted, arXiv:astro-ph/0703571

Rusin, D., Kochanek, C. S., Falco, E. E., Keeton, C. R., McLeod, B. A., Impey, C. D., Lehár, J., Muñoz, J. A., Peng, C. Y., & Rix, H.-W. 2003, ApJ, 587, 143

Sanderson, A. J. R. & Ponman, T. J. 2004, in Clusters of Galaxies: Probes of Cosmological Structure and Galaxy Evolution, ed. J. S. Mulchaey, A. Dressler, & A. Oemler

Schmidt, R. W. & Allen, S. W. 2007, MNRAS, 379, 209

Seljak, U. 2000, MNRAS, 318, 203

Seljak, U. & Warren, M. S. 2004a, MNRAS, 355, 129

—. 2004b, MNRAS, 355, 129

Seljak, U. et al. 2005, Phys. Rev. D, 71, 043511

Sheldon, E. S., Johnston, D. E., Frieman, J. A., et al. 2004, AJ, 127, 2544

Sheldon, E. S., Johnston, D. E., Scranton, R., Koester, B., McKay, T., Oyaizu, H., Cunha, C., Lima, M., Lin, H., Frieman, J., Wechsler, R. H., Annis, J., Mandelbaum, R., Bahcall, N. A., & Fukugita, F. 2007, ApJ, submitted

Sheth, R. K., Mo, H. J., & Tormen, G. 2001, MNRAS, 323, 1

Sheth, R. K. & Tormen, G. 1999, MNRAS, 308, 119

Smith, R. E., Scoccimarro, R., & Sheth, R. K. 2007, Phys. Rev. D, 75, 063512

SNAP Collaboration. 2005, ArXiv Astrophysics e-prints, astro-ph/0507460

Spergel, D. N., Bean, R., Doré, O., Nolta, M. R., Bennett, C. L., Dunkley, J., Hinshaw, G., Jarosik, N., Komatsu, E., Page, L., Peiris, H. V., Verde, L., Halpern, M., Hill, R. S., Kogut, A., Limon, M., Meyer, S. S., Odegard, N., Tucker, G. S., Weiland, J. L., Wollack, E., & Wright, E. L. 2007, ApJS, 170, 377

Springel, V., White, S. D. M., Jenkins, A., Frenk, C. S., Yoshida, N., Gao, L., Navarro, J., Thacker, R., Croton, D., Helly, J., Peacock, J. A., Cole, S., Thomas, P., Couchman, H., Evrard, A., Colberg, J., & Pearce, F. 2005, Nature, 435, 629

Tinker, J. L., Weinberg, D. H., Zheng, Z., & Zehavi, I. 2005, ApJ, 631, 41

Tyson, J. A. & Fischer, P. 1995, ApJ, 446, L55

Tyson, J. A., Valdes, F., Jarvis, J. F., & Mills, A. P. 1984, ApJ, 281, L59

Tyson, J. A., Wittman, D. M., Hennawi, J. F., & Spergel, D. N. 2002, LSST: a Complementary Probe of Dark Energy

Vale, C. & White, M. 2006, New Astronomy, 11, 207

Viana, P. T. P. & Liddle, A. R. 1999, MNRAS, 303, 535

Warren, M. S., Abazajian, K., Holz, D. E., & Teodoro, L. 2006, ApJ, 646, 881

Wechsler, R. H., Bullock, J. S., Primack, J. R., Kravtsov, A. V., & Dekel, A. 2002, ApJ, 568, 52

Wechsler, R. H., Zentner, A. R., Bullock, J. S., Kravtsov, A. V., & Allgood, B. 2006, ApJ, 652, 71

Wetzel, A. R., Cohn, J. D., White, M., Holz, D. E., & Warren, M. S. 2007, ApJ, 656, 139

White, S. D. M., Efstathiou, G., & Frenk, C. S. 1993, MNRAS, 262, 1023

Wright, C. O. & Brainerd, T. G. 2000, ApJ, 534, 34

Yang, X., Mo, H. J., van den Bosch, F. C., Jing, Y. P., Weinmann, S. M., & Meneghetti, M. 2006, MNRAS, 1233

Yee, H. K. C., Morris, S. L., Lin, H., Carlberg, R. G. an Hall, P. B., Sawicki, M., Patton, D. R., Wirth, G. D., Ellingson, E., & Shepherd, C. W. 2001, VizieR Online Data Catalog, 212, 90475

York, D. G. et al. 2000, AJ, 120, 1579

Zehavi, I. et al. 2004, ApJ, 608, 16

Zehavi, I., et al. 2005, ApJ, 630, 1

Zheng, Z. 2004, ApJ, 610, 61